Annual Report # 1 for NSF Proposal: DMS 16-20231

Period of Performance: 2016-2017

Title: A Hierarchical Multiscale Method for Nonlocal Fine-scale Models via Merging Weak Galerkin and VMS Frameworks

PI: Arif Masud
University of Illinois at Urbana-Champaign

Focus of Year-1 (2016-2017): Development of Variationally Consistent Method for Weak and Strong Discontinuities in Multi-Constituent Materials

Executive Summary of Year 1 Effort

A stabilized interface formulation is developed for strong discontinuity at finite strains across general bimaterial interfaces by embedding stabilized Discontinuous Galerkin (DG) ideas in the Continuous Galerkin method. Introducing an interfacial gap function that evolves subject to constraints imposed by opening and/or sliding interfaces, the proposed Variational Multiscale DG (VMDG) method seamlessly tracks strong discontinuity and interface debonding by treating damage and friction in a unified way. An internal variable formalism together with the notion of irreversibility of damage results in a set of evolution equations for the gap function. Evolution of the debonding surfaces requires interfacial stabilization that is developed based on residual-based stabilization concepts. Tension debonding, compression damage, and frictional sliding are accommodated, and return mapping algorithms in the presence of evolving strong discontinuities are developed. A significant contribution in this work is the consistently derived method to model the Lagrange multiplier field via interfacial flux and jump terms and variational embedding of various nonlinear interfacial debonding models at the interfacial boundaries. This derivation variationally embeds the interfacial kinematic models that are crucial to capturing the physical and mathematical properties involving large stains and damage. A set of representative test cases highlight the salient features of the proposed VMDG method and confirm its robustness and range of applicability.

1. Introduction

Accurate modeling of evolving discontinuity and interfacial debonding that leads to local failure in natural and engineered material systems constitutes an essential building block for high

fidelity computational material modeling frameworks. A common classical approach for this class of problems that involve local failure and separation is the use of intrinsic cohesive elements or springs along the bimaterial interfaces; see e.g. [1,6,15,17,39]. It is however well documented in the literature that these formulations typically introduce an additional elastic stiffness at the interface that upsets the consistency of the discrete formulation, thereby resulting in inaccurately representation of the multi-material interfacial configuration. Numerical tests show that loss of consistency can result in serious degradation in the accuracy of the simulations [6]. As an alternative approach that avoids artificial compliance, the extrinsic cohesive zone method [7,20,26,53] adaptively inserts interface elements into contiguous meshes when a fracture criteria is met in the neighboring solid elements. Later developments [49] using the extended finite element method (XFEM) enable the failure surface to grow through elements. However, the insertion of cohesive elements adds degrees of freedom to the global stiffness matrix, requiring special data structures for adaptivity in the finite element software.

On the other hand, kinematic treatment of embedded interfaces has been carried out in the context of Lagrange multiplier methods [14,20], as well as Nitsche type methods [1,2,11,12,10,13,34] that can be categorized as a class of primal methods [8]. Lagrange multiplier based methods, though general, and applicable to linear as well as nonlinear material systems, render the resulting method a mixed-field method. Numerical schemes for mixed-field methods require stabilized methods if arbitrary combinations of interpolation functions are to be employed for the underlying fields. Nitsche type methods on the other hand do not introduce an additional field to be approximated, but they require specification of interfacial continuity parameters which are not always easy to define especially in the general nonlinear regime [10].

A third approach for the treatment of the failure models is based on the hybrid DG method [25,30,35] which has also been employed in fracture mechanics [32,52]. In this approach, discontinuous Galerkin (DG) method is used in the pre-failure regime together with a standard cohesive zone approximation to perform the post-failure process. In this particular method, the stiffness matrix and the underlying mathematical formulation changes when switching from the pre-failure to post-failure regime. Yet another approach by Belytschko and coworkers [52], employs Cohesive Zone Method (CZM) embedded in the XFEM method to model transition between perfectly adhered to fully debonded regimes via some properly chosen enrichment functions. This approach requires carefully selected point-wise consistency conditions for the initiation of the new degree of freedom [52].

With the objective of developing a general framework for local failure at material interfaces, we derived a Lagrange multiplier method, in the context of small strains, for continuity of fields across embedded interfaces [44]. In this method Lagrange multipliers manifested interfacial traction field. This idea was further enhanced in [43] wherein interfacial Lagrange multiplier as well as the penalty parameters were fully derived via sub-scale modeling concept facilitated by

the VMS ideas [16,22]. In an allied effort a finite strain interface formulation for multi-material interfaces in the finite strain regime was developed by us in [42]. However local failure in the form of strong discontinuity was not considered. Numerical tests with primal interfacial formulation [42] revealed that the success of the method in the finite strain regime relied heavily on the consistent evolution of the interfacial stabilization parameters, and consequently, the variational structure of the sub-grid scale modeling problem was crucial to the derivation presented. This paper builds on Lagrange multiplier enforcement of continuity and derivation of Nitsche parameters in [44] with variationally consistent derivation of interfacial stabilization parameters in [42] for local interfacial failure and appearance of strong discontinuities. A crucial component of this derivation is the modeling of fine scales in the neighborhood of element interfaces. These ideas have similarities with certain aspects of Weak Galerkin methods by Wang and co-workers [27-29, 50]. Weak Galerkin method makes use of discontinuous functions that endows WG-FEMs with great flexibility to deal with geometric complexities and boundary conditions. These methods have been applied to interface problems [28] wherein flexibility of using discontinuous functions gives rise to robustness in the enforcement of interface jump conditions and therefore has been used to develop methods for handling discontinuous approximation functions. However, while the edge restricted functions that are used in Weak Galerkin appear similar to the fine scale field in the present formulation, the derived solution of the fine scale problem depends on the interior support of the fine-scale field.

To keep the discussion self-contained, we first present the synopsis of the stabilized formulation for finite strain interface without damage [42]. We then introduce the notion of inelastic residual gap ζ in the formulation to restrict the continuity along the interface. The key underlying idea is that the residual gap or separation along the interface is treated as an irrecoverable or inelastic strain-like variable which evolves with the debonding process. We then present a thermodynamically consistent formulation analogous to the variational constructs for bulk domain inelasticity discussed in [36] wherein the residual gap ζ is conjugate to the interface traction T, thereby incorporating hardening/softening variables. This methodology is a slight departure from the method of [44] and enables the treatment of interface constitutive behavior through yield functions and flow rules that are inspired by the literature from plasticity. In the present method the combination of damage and friction along the debonding surfaces is easily accommodated by borrowing concepts from multi-surface plasticity [36]. Also, rate dependency and other advanced phenomena can be easily treated in the new framework. Specially, the proposed method avoids using cohesive elements that can introduce artificial elastic interface stiffness that affects the consistency and therefore the stability of the method. With the fine-scale models evolving with the material and geometric nonlinearity exhibited in the vicinity of the interface, the algorithmic interface parameters are updated continuously through the evolution of the nonlinear problem. Furthermore, the proposed method provides a general framework to incorporate friction, rate-dependency, and softening, as desired.

An outline of the report is as follows. In section 2, we begin with the governing equations of finite strain elasticity with strong discontinuity and an internal variable ζ associated with damage. Next, we derive the stabilized weak form for interfacial debonding in multi-constituent materials by employing the sub-grid scale modeling concept facilitated by the VMS method, but restricted to narrow zone across the bimaterial interfaces. In section 4, the appearance of the gap function in the expression for the Lagrange multiplier and therefore in the evolving finite-scales provides a natural mechanism to embed physics based models [23,44] as well as phenomenological models [42,46] for progressive failure under various loading scenarios [1,44]. In section 5, specifically, tension debonding and evolution of normal gap, and compressive frictional sliding are presented and algorithmic generalizations are developed. Corresponding return mapping algorithms that are motivated by the literature on computational inelasticity [36] are discussed. An essential ingredient for a robust numerical method for finite deformation kinematics in the finite strain regime is the derivation of the consistent tangent that can yield quadratic convergence when employed in conjunction with the Newton-Raphson scheme. Therefore, Section 6 presents consistent linearization of the stabilized method. Finally, Section 7 presents a series of numerical test cases that validate the method and show its range of applicability.

2.   Governing Equations and Interfacial Weak Form for Strong Discontinuity

Evolving interfaces between elements in the finite deformation context, where interfaces not only undergo finite deformation but can also develop interfacial gaps, are shown in Figure 1. Our earlier work in [42] presents the equilibrium equations at finite strains, but with no openings or gaps. Further extensions to frictional interace dynamics are presented in [46]. Interested readers are referred to these two papers for detailed discussions. In this work, an open bounded region $\Omega \subset \mathbb{R}^{n_{sd}}$ is cut into two disjoint regions $\Omega^{(1)}$ and $\Omega^{(2)}$ by an interface Γ_{I}. Points in the reference configuration are denoted by $X \in \Omega^{(1)} \bigcup \Omega^{(2)}$ and their corresponding images in the current configuration by x. Herein, the superscript (α) denotes quantities appearing in both regions 1 and 2. The two bodies deform according to the motion $\boldsymbol{\phi}^{(\alpha)}(X,t)$ that maps the reference configuration onto the current configuration, $x = \boldsymbol{\phi}^{(\alpha)}(X,t)$.

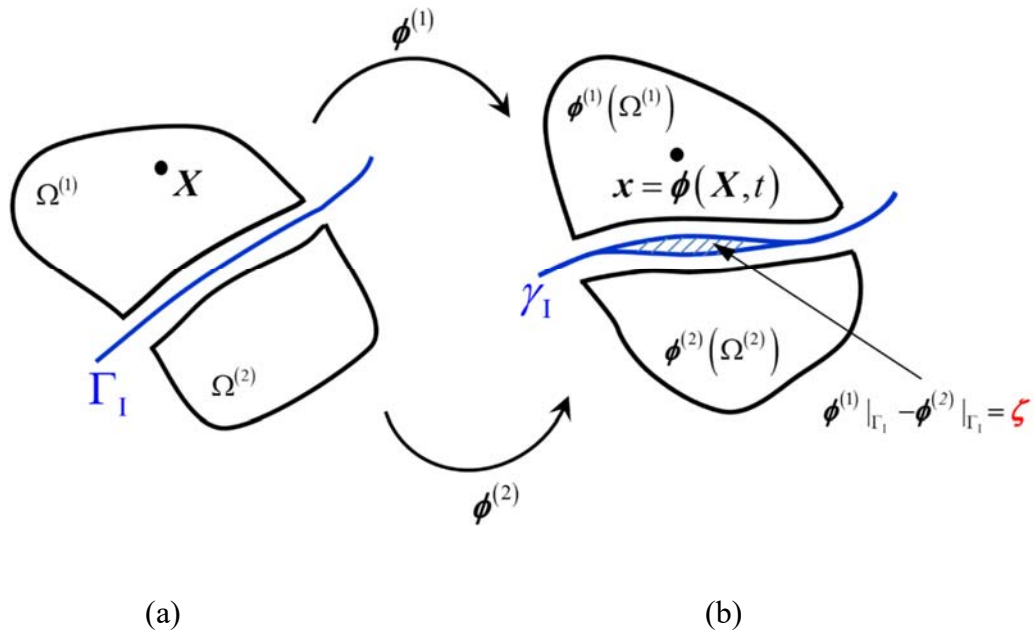(a)   (b)

Figure 1. Domain Ω with interface Γ_I. The deformed configurations are given by $\boldsymbol{\phi}^{(1)}$ and $\boldsymbol{\phi}^{(2)}$: (a) Reference configuration; (b) Current configuration.

We allow the deformations $\boldsymbol{\phi}^{(\alpha)}$ to be distinct along the interface Γ_I to accommodate the existence of the interface gap or debonding ζ as illustrated in Figure 1-b. The interior domains $\Omega^{(1)}$ and $\Omega^{(2)}$ remain self-compatible and self-equilibrated within each sub-region. Equilibrium equations and boundary conditions for each sub-region $\Omega^{(\alpha)}$ are supplemented with the discontinuity evolution equation and the traction conditions along Γ_I via the Lagrange multiplier field $\boldsymbol{\lambda}$, thereby resulting in the following system of equations for the composite domain Ω.

$$\mathrm{DIV}\,\boldsymbol{P}^{(\alpha)}\left(\boldsymbol{F}^{(\alpha)}\right)+\rho_o^{(\alpha)}\boldsymbol{B}^{(\alpha)}=\boldsymbol{0} \qquad \text{in}\quad \Omega^{(\alpha)},\ \alpha=1,2 \tag{1}$$

$$\boldsymbol{\phi}^{(\alpha)}=\boldsymbol{X}^{(\alpha)} \qquad\qquad\qquad \text{on}\ \Gamma^{(\alpha)}\setminus\Gamma_\mathrm{I},\ \alpha=1,2 \tag{2}$$

$$\boldsymbol{\phi}^{(1)}-\boldsymbol{\phi}^{(2)}=\boldsymbol{\zeta} \qquad\qquad\qquad \text{on}\ \Gamma_\mathrm{I} \tag{3}$$

$$\boldsymbol{\lambda}-\boldsymbol{P}^{(1)}\cdot\boldsymbol{N}^{(1)}=\boldsymbol{0} \qquad\qquad \text{on}\ \Gamma_\mathrm{I} \tag{4}$$

$$-\boldsymbol{P}^{(2)}\cdot\boldsymbol{N}^{(2)}-\boldsymbol{\lambda}=\boldsymbol{0} \qquad\qquad \text{on}\ \Gamma_\mathrm{I} \tag{5}$$

Equation (3) facilitates non-conforming evolution of the interfaces that are subject to impenetrability constraint and phenomenological and/or physics based interfacial kinematics. In (1) to (5), $P^{(\alpha)}$ is the first Piola-Kirchhoff stress tensor, $B^{(\alpha)}$ is the body force vector, $\rho_o^{(\alpha)}$ is the mass density, and $N^{(\alpha)}$ is the unit outward normal vector at the region boundary Γ_{I}. Homogeneous Dirichlet boundary conditions are applied for simplicity of presentation but they can be easily generalized [42]. Lagrange multiplier λ is introduced to enforce the equilibrium of tractions (4) – (5) while the two subdomains are fully or partially bonded; the multipliers vanish identically upon complete debonding. The case of multiple interfaces can be accommodated by a straightforward generalization.

Multiplying equilibrium equations (1) to (5) by weighting function $\eta_o^{(\alpha)}$ and applying the divergence theorem, the associated weak form is expressed as follows: Find $\left\{ \phi^{(1)}, \phi^{(2)}, \lambda \right\} \in \mathcal{S}^{(1)} \times \mathcal{S}^{(2)} \times \mathcal{Q}$ such that for all $\left\{ \eta_o^{(1)}, \eta_o^{(2)}, \mu \right\} \in \mathcal{V}^{(1)} \times \mathcal{V}^{(2)} \times \mathcal{Q}$:

$$\sum_{\alpha=1}^{2} \int_{\Omega^{(\alpha)}} \mathrm{GRAD}\, \eta_o^{(\alpha)} : P^{(\alpha)} \, \mathrm{d}V - \sum_{\alpha=1}^{2} \int_{\Omega^{(\alpha)}} \rho_o^{(\alpha)} B^{(\alpha)} \cdot \eta_o^{(\alpha)} \, \mathrm{d}V - \int_{\Gamma_{\mathrm{I}}} \lambda \cdot [\![\eta_o]\!] \, \mathrm{d}A = 0 \tag{6}$$

$$-\int_{\Gamma_{\mathrm{I}}} \mu \cdot \left([\![\phi]\!] - \zeta \right) \mathrm{d}A = 0 \tag{7}$$

As mentioned earlier in [42], the Lagrange multiplier field λ in (6) has the connotation of the traction field on Γ_{I}. Eqn. (7) weakly enforces the jump continuity where $[\![\bullet]\!] = (\bullet)^{(1)} - (\bullet)^{(2)}$ is the jump operator defined for vector-valued fields at interface Γ_{I}. The inelastic gap function or debonding function ζ is set to lie in the $\left[L_2 (\Gamma_{\mathrm{I}}) \right]^{n_{\mathrm{sd}}}$ space. The appropriate function spaces contained in the weak forms (6) and (7) are given as:

$$\mathcal{S}^{(\alpha)} = \left\{ \phi^{(\alpha)} \,\middle|\, \phi^{(\alpha)} \in \left[H^1 (\Omega^{(\alpha)}) \right]^{n_{\mathrm{sd}}}, \, \det\left(F^{(\alpha)} (\phi^{(\alpha)}) \right) > 0, \, \phi^{(\alpha)} \big|_{\Gamma^{(\alpha)} \backslash \Gamma_{\mathrm{I}}} = X^{(\alpha)} \right\} \tag{8}$$

$$\mathcal{V}^{(\alpha)} = \left\{ \eta_o^{(\alpha)} \,\middle|\, \eta_o^{(\alpha)} \in \left[H_o^1 (\Omega^{(\alpha)}) \right]^{n_{\mathrm{sd}}}, \, \eta_o^{(\alpha)} \big|_{\Gamma^{(\alpha)} \backslash \Gamma_{\mathrm{I}}} = 0 \right\} \tag{9}$$

$$\mathcal{Q} = \left\{ \lambda \,\middle|\, \lambda \in \left[H^{-\frac{1}{2}} (\Gamma_{\mathrm{I}}) \right]^{n_{\mathrm{sd}}} \right\} \tag{10}$$

3. Multiscale decomposition

Our objective at this point is to convert the preceding Lagrange multiplier formulation (6) and (7) into a stabilized single-field formulation for the evolution of interfacial debonding in the finite deformation context. Interested reader is referred to [42] for details of the primal

interface formulation without damage and for the advantages of the single field formulation in the context of the inf-sup stability conditions. For the sake of completeness, we highlight the significant steps to variationally derive the method for evolving gaps and debonding.

Following the work in [24,42], we decompose the solution field into coarse-scale and fine-scale fields. We assume an overlapping decomposition of the deformation map $\boldsymbol{\phi}^{(\alpha)}$ in each region $\Omega^{(\alpha)}$ consisting of a fine-scale deformation $\tilde{\boldsymbol{\phi}}^{(\alpha)}$ superimposed upon a coarse-scale deformation $\hat{\boldsymbol{\phi}}^{(\alpha)}$. This deformation can be expressed in terms of the multiscale displacement field as follows:

$$\hat{\boldsymbol{x}} = \hat{\boldsymbol{\phi}}(\boldsymbol{X}) = \boldsymbol{X} + \hat{\boldsymbol{u}} \tag{11}$$

$$\tilde{\boldsymbol{\phi}}(\hat{\boldsymbol{x}},t) = \hat{\boldsymbol{x}} + \tilde{\boldsymbol{u}} = \boldsymbol{\phi}(\boldsymbol{X},t) = \boldsymbol{X} + \boldsymbol{u} = \boldsymbol{x} \tag{12}$$

From (11) and (12), we arrive at a relation between the total displacement and its coarse and fine-scale displacement components as follows:

$$\boldsymbol{u} = \hat{\boldsymbol{u}} + \tilde{\boldsymbol{u}} \tag{13}$$

As in our recent developments [23], the coarse-scale field $\hat{\boldsymbol{\phi}}^{(\alpha)}$ is represented using piecewise continuous finite element functions in each region $\Omega^{(\alpha)}$, and the fine-scale field $\tilde{\boldsymbol{\phi}}^{(\alpha)}$ is represented locally at the interfaces via functions of compact support.

Although the displacement field is assumed additively decomposed, and in the nonlinear regime this decomposition is to be viewed in the sense of mappings, the Lagrange multiplier fields are not decomposed. Therefore weak enforcement of jump continuity only contributes to the coarse-scale model. Accordingly, the weak forms (6) and (7) can be separated into the following multiscale interface sub-problems:

Coarse-Scale Problem $\mathcal{C}$

$$\hat{R}\left(\hat{\boldsymbol{\eta}}_o^{(\alpha)}; \hat{\boldsymbol{\phi}}^{(\alpha)}, \tilde{\boldsymbol{\phi}}^{(\alpha)}, \boldsymbol{\lambda}\right) = \sum_{\alpha=1}^{2} \int_{\Omega^{(\alpha)}} \left[\text{GRAD}\, \hat{\boldsymbol{\eta}}_o^{(\alpha)} : \boldsymbol{P}^{(\alpha)} - \hat{\boldsymbol{\eta}}_o^{(\alpha)} \cdot \rho_o^{(\alpha)} \boldsymbol{B}^{(\alpha)} \right] \mathrm{d}V$$
$$- \int_{\Gamma_{\mathrm{I}}} \boldsymbol{\lambda} \cdot [\![\hat{\boldsymbol{\eta}}_o]\!]\, \mathrm{d}A = 0 \tag{14}$$

$$\hat{R}_{\mu}\left(\boldsymbol{\mu}, \hat{\boldsymbol{\phi}}^{(\alpha)}, \tilde{\boldsymbol{\phi}}^{(\alpha)}, \boldsymbol{\zeta}\right) = -\int_{\Gamma_{\mathrm{I}}} \boldsymbol{\mu} \cdot \left([\![\tilde{\boldsymbol{\phi}} \circ \hat{\boldsymbol{\phi}}]\!] - \boldsymbol{\zeta}\right) \mathrm{d}A = 0 \tag{15}$$

Fine-Scale Problem $\mathcal{F}$

$$\tilde{R}\left(\tilde{\boldsymbol{\eta}}_o^{(\alpha)}; \hat{\boldsymbol{\phi}}^{(\alpha)}, \tilde{\boldsymbol{\phi}}^{(\alpha)}, \lambda\right) = \sum_{\alpha=1}^{2} \int_{\Omega^{(\alpha)}} \left[\text{GRAD}\, \tilde{\boldsymbol{\eta}}_o^{(\alpha)} : \boldsymbol{P}^{(\alpha)} - \tilde{\boldsymbol{\eta}}_o^{(\alpha)} \cdot \rho_o^{(\alpha)} \boldsymbol{B}^{(\alpha)} \right] dV$$

$$- \int_{\Gamma_I} \lambda \cdot [\![\tilde{\boldsymbol{\eta}}_o]\!]\, dA = 0 \tag{16}$$

As discussed in [42], our objective at this point is to derive an analytical expression for Lagrange multipliers in terms of the coarse-scale deformation map $\hat{\boldsymbol{\phi}}^{(\alpha)}$ and the inelastic gap ζ as the two unknown fields. The detailed procedure is provided in [42], which is comprised of three step modeling process. In the following sections we outline the main steps of the modeling process.

3.1.   Modeling of fine scales

We localize the fine-scale problem (16) to the vicinity of the interface and approximate the fine scales using edge bubble functions that are only supported within the sectors next to the interface segments. We express fine scales via edge bubble functions as follows:

$$\tilde{\boldsymbol{\phi}}^{(\alpha)} = \boldsymbol{\beta}_s^{(\alpha)} b_s^{(\alpha)}, \qquad\qquad \tilde{\boldsymbol{\eta}}_o^{(\alpha)} = \boldsymbol{\gamma}_s^{(\alpha)} b_s^{(\alpha)} \tag{17}$$

In the interest of brevity, the reader is referred to [42] for the details on the localization procedure. The method proposed in [42] is general and therefore applicable to nonconforming meshes as well. However, our present work on evolving debonding is particular to conforming meshes, so the segments are simply the intersecting/adjacent element boundaries.

The next step is the linearization of (16) with respect to the fine scales $\tilde{\boldsymbol{\phi}}^{(\alpha)}$. Because the fine scales are localized to the interface, after the linearization of (16), the fine-scale field is treated as an incremental displacement $\Delta \tilde{\boldsymbol{u}}^{(\alpha)}$ field about the coarse-scale deformation $\hat{\boldsymbol{\phi}}^{(\alpha)}$ along the interface:

$$\sum_{\alpha=1}^{2} \int_{\omega^{(\alpha)}} \text{GRAD}\, \tilde{\boldsymbol{\eta}}_o^{(\alpha)} : \mathbf{A}^{(\alpha)}\left(\boldsymbol{F}^{(\alpha)}\right) : \text{GRAD}\, \Delta \tilde{\boldsymbol{u}}^{(\alpha)}\, dV = -\tilde{R}_s\left(\hat{\boldsymbol{\eta}}_o^{(\alpha)}; \hat{\boldsymbol{\phi}}^{(\alpha)}, \mathbf{0}, \lambda\right) \tag{18}$$

where the acoustic tensor of material moduli $\mathbf{A}^{(\alpha)}\left(\boldsymbol{F}^{(\alpha)}\right)$ is defined as:

$$\mathbf{A}^{(\alpha)}\left(\boldsymbol{F}^{(\alpha)}\right) = \frac{\partial^2 W^{(\alpha)}}{\partial \boldsymbol{F} \partial \boldsymbol{F}} \tag{19}$$

We solve (18) by substituting the expression for fine scales (17). The detailed procedures for solving the fine-scale solution are provided in [42]. A key property of the method is that the expression for the fine-scale solution $\Delta \tilde{\boldsymbol{u}}^{(\alpha)}$ remains unchanged when compared with [42]:

$$\Delta \tilde{\boldsymbol{u}}^{(\alpha)} = \boldsymbol{\tau}_s^{(\alpha)} \cdot \left[(-1)^{\alpha-1} \boldsymbol{\lambda} - \boldsymbol{P}^{(\alpha)} \cdot \boldsymbol{N}^{(\alpha)} \right] \tag{20}$$

where:

$$\boldsymbol{\tau}_s^{(\alpha)} = \left[\text{meas} \left(\gamma_s \right) \right]^{-1} \left(\int_{\gamma_s} b_s^{(\alpha)} \, \mathrm{d}A \right)^2 \tilde{\boldsymbol{\tau}}_s^{(\alpha)} \tag{21}$$

$$\tilde{\boldsymbol{\tau}}_s^{(\alpha)} = \left[\int_{\omega_s^{(\alpha)}} \mathrm{GRAD} \, b_s^{(\alpha)} : \mathbf{A}^{(\alpha)} : \mathrm{GRAD} \, b_s^{(\alpha)} \, \mathrm{d}V \right]^{-1} \tag{22}$$

An important point to note is that the residual based fine-scale solution incorporates the effects of evolving geometric and material nonlinearity on either side of the interface via the acoustic tensor $\mathbf{A}^{(\alpha)} \left(\boldsymbol{F}^{(\alpha)} \right)$ that appears in the expression for the stability tensors $\tilde{\boldsymbol{\tau}}_s^{(\alpha)}$ [42]. These dependencies play a key role in the properties of the numerical flux derived below.

Remark. The fine-scale derivation is based on a two-step process: localization and then linearization, as in [42] and [43] in the finite strain regime. One can also refer to [45] for evolution of the fine scales for different PDEs. The distinction emerges in the derived form of the Lagrange multipliers that account for the gap function ζ.

3.2. Variational embedding in the coarse-scale problem with strong discontinuity

We now focus on the continuity equation (15) in order to obtain an expression for the Lagrange multiplier field λ. Following [42, 46], we substitute the fine-scale model (20) and the multiscale decomposition (11) – (13) into (15). Assuring L_2 projection of λ and locally satisfying the resulting equation for all values of the multiplier μ, an explicit form is obtained for the interfacial traction λ:

$$\lambda = \left[\boldsymbol{\delta}_s^{(1)} \cdot \boldsymbol{P}^{(1)} \cdot \boldsymbol{N}^{(1)} - \boldsymbol{\delta}_s^{(2)} \cdot \boldsymbol{P}^{(2)} \cdot \boldsymbol{N}^{(2)} \right] - \boldsymbol{\tau}_s \cdot \left(\left[\!\left[\hat{\boldsymbol{\phi}} \right]\!\right] - \boldsymbol{\zeta} \right) \tag{23}$$

where $\boldsymbol{\delta}_s^{(\alpha)} = \boldsymbol{\tau}_s \cdot \boldsymbol{\tau}_s^{(\alpha)}$ is the flux weighting tensor consisting of the stabilization tensor from both subdomains, and $\boldsymbol{\tau}_s = \left(\boldsymbol{\tau}_s^{(1)} + \boldsymbol{\tau}_s^{(2)} \right)^{-1}$.

By substituting λ into (20), a simplified expression for the fine scales results is as follows:

$$\Delta \tilde{\boldsymbol{u}}^{(\alpha)} = -\boldsymbol{\delta}_s \left[\boldsymbol{P}^{(1)} \cdot \boldsymbol{N}^{(1)} + \boldsymbol{P}^{(2)} \cdot \boldsymbol{N}^{(2)} \right] + (-1)^{\alpha} \, \boldsymbol{\delta}_s^{(\alpha)T} \cdot \left(\left[\!\left[\hat{\boldsymbol{\phi}} \right]\!\right] - \boldsymbol{\zeta} \right) \tag{24}$$

where the last term contains the inelastic gap term, which is a significantly distinct feature as compared to the expression for the fine-scale field in [42]. Furthermore, the symmetry of the tensors $\boldsymbol{\tau}_s^{(\alpha)}$ and $\boldsymbol{\tau}_s$ has been employed to enable the substitution $\boldsymbol{\delta}_s^{(\alpha)T} = \boldsymbol{\tau}_s^{(\alpha)} \cdot \boldsymbol{\tau}_s$. Also, the additional stability tensor $\boldsymbol{\delta}_s$ in (24) is form identical to the one in [42]:

$$\boldsymbol{\delta}_s = \boldsymbol{\tau}_s^{(1)} \cdot \boldsymbol{\delta}_s^{(2)} = \boldsymbol{\tau}_s^{(2)} \cdot \boldsymbol{\delta}_s^{(1)} \tag{25}$$

It is important to note that the expression for Lagrange multiplier λ naturally accommodates the gap function ζ. Since evolution of gap function is governed by kinematic constraint conditions in addition to evolution models dictating the evolution of ζ, the micromechanical physics manifested via these models is fully embedded in expression (24) for λ. This is a significant contribution of the present work and sets it apart from any numerical methods that have been proposed for interfacial kinematics of finitely deforming embedded interfaces with evolving gaps and discontinuities. Namely, the consistently derived numerical flux λ contains a-priori the ability to represent strong discontinuities, rather than methods which transition to debonding by adaptively inserting interface elements as in extrinsic methods or by changing algorithmic parameters from 0 to 1 as in hybrid methods. We wish to emphasize that the proposed consistent derivation that variationally embeds the interfacial kinematic models is crucial to the derivation of consistent tangent tensors that are fundamental to obtaining quadratic convergence rates when employed in the Newton Raphson method.

Remark. Note that by adding the inelastic gap ζ function in (3), the first term in (24) which is the average traction term does not change with respect to the form presented in [42]. Furthermore, the structural form of the stability tensor $\boldsymbol{\tau}_s$ and the fine-scale stabilization tensor $\boldsymbol{\tau}_s^{(\alpha)}$ are not altered by the introduction of the ζ term. Short of the strong discontinuity capturing term ζ, the structure of the interface stabilizing terms can be traced through the VMS derivation back to the Galerkin least-squares inspired methods in the linear field context [4,9].

Incorporating the expressions for λ (23) and the fine-scale fields $\Delta \tilde{\boldsymbol{u}}^{(\alpha)}$ (24) in the linearized coarse-scale problem (14) yields the following stabilized interface formulation for finite deformations:

$$
\begin{aligned}
R\left(\boldsymbol{\eta}_o^{(\alpha)}, \boldsymbol{\phi}^{(\alpha)}\right) &= \sum_{\alpha=1}^{2} \int_{\Omega^{(\alpha)}} \left[\operatorname{GRAD} \boldsymbol{\eta}_o^{(\alpha)} : \boldsymbol{P}^{(\alpha)} - \boldsymbol{\eta}_o^{(\alpha)} \cdot \rho_o^{(\alpha)} \boldsymbol{B}^{(\alpha)} \right] \mathrm{d}V \\
&\quad - \int_{\Gamma_I} [\![\boldsymbol{\eta}_o]\!] \cdot \{ \boldsymbol{P} \cdot \boldsymbol{N} \} \, \mathrm{d}A - \int_{\Gamma_I} \left\{ (\operatorname{GRAD} \boldsymbol{\eta}_o : \boldsymbol{A}) \cdot \boldsymbol{N} \right\} \cdot \left([\![\boldsymbol{\phi}]\!] - \zeta \right) \mathrm{d}A \\
&\quad + \int_{\Gamma_I} [\![\boldsymbol{\eta}_o]\!] \cdot \boldsymbol{\tau}_s \cdot \left([\![\boldsymbol{\phi}]\!] - \zeta \right) \mathrm{d}A - \int_{\Gamma_I} [\![(\operatorname{GRAD} \boldsymbol{\eta}_o : \boldsymbol{A}) \cdot \boldsymbol{N}]\!] \cdot \boldsymbol{\delta}_s \cdot [\![\boldsymbol{P} \cdot \boldsymbol{N}]\!] \, \mathrm{d}A = 0
\end{aligned}
\tag{26}
$$

where $\boldsymbol{\delta}_s = \left[\left(\boldsymbol{\tau}_s^{(1)} \right)^{-1} + \left(\boldsymbol{\tau}_s^{(2)} \right)^{-1} \right]^{-1}$ is the derived stability tensor for the traction jump term,

$\{ (\bullet) \cdot \boldsymbol{N} \} = (\bullet)^{(1)} \cdot \boldsymbol{N}^{(1)} - (\bullet)^{(2)} \cdot \boldsymbol{N}^{(2)}$ is the defined as the weighted average flux operator, and

$[\![(\bullet) \cdot \boldsymbol{N}]\!] = (\bullet)^{(1)} \cdot \boldsymbol{N}^{(1)} + (\bullet)^{(2)} \cdot \boldsymbol{N}^{(2)}$ is defined as the jump operator. The traction jump term,

which emerges also in previous derivations for small strain [45,46] and large strain [42], is a distinguishing feature with respect to Nitsche and interior penalty Discontinuous Galerkin formulations for small [2,3,34] and large [31] strains. We remark that this term is most significant when the traction jump $[\![\boldsymbol{P} \cdot \boldsymbol{N}]\!]$ is large, such as models with large material mismatch or element size changes across an interface. However, we choose to simplify the formulation by neglecting this term as in [42,46], leading to a formulation structurally similar to typical DG methods with all parameters consistently derived:

$$
\begin{aligned}
R\left(\boldsymbol{\eta}_o^{(\alpha)}, \boldsymbol{\phi}^{(\alpha)}\right) = \sum_{\alpha=1}^{2} \int_{\Omega^{(\alpha)}} \Big[\operatorname{GRAD} \boldsymbol{\eta}_o^{(\alpha)} : \boldsymbol{P}^{(\alpha)} - \boldsymbol{\eta}_o^{(\alpha)} \cdot \rho_o^{(\alpha)} \boldsymbol{B}^{(\alpha)} \Big] \mathrm{d}V \\
- \int_{\Gamma_I} [\![\boldsymbol{\eta}_o]\!] \cdot \{ \boldsymbol{P} \cdot \boldsymbol{N} \} \, \mathrm{d}A - \int_{\Gamma_I} \{ (\operatorname{GRAD} \boldsymbol{\eta}_o : \boldsymbol{A}) \cdot \boldsymbol{N} \} \cdot ([\![\boldsymbol{\phi}]\!] - \boldsymbol{\zeta}) \, \mathrm{d}A \\
+ \int_{\Gamma_I} [\![\boldsymbol{\eta}_o]\!] \cdot \boldsymbol{\tau}_s \cdot ([\![\boldsymbol{\phi}]\!] - \boldsymbol{\zeta}) \, \mathrm{d}A = 0
\end{aligned}
\tag{27}
$$

The stabilized residual form (27) has the inelastic gap $\boldsymbol{\zeta}$ term inside the integral expression which plays a key role in the evolution of strong discontinuity or interfacial damage. Variationally consistent updating of these stabilization tensors results in a stabilized formulation that leads to a robust numerical method as shown via numerical test cases in Section 7.

Remark. *The interface formulation presented in (27) is symmetric. For further simplification of the residual form (27), the interested reader is referred to [43] which suggests several generalizations along with insights into the efficiency of such modifications.*

Remark. *The present derivations are restricted to hyperelastic material response in each solid domain* $\Omega^{(\alpha)}$*. Material inelasticity can be accommodated by extending the developments in [47] for a symmetric, small strain, elastoplastic DG method.*

Remark. *As seen in (24) the numerical flux contains a priori the ability to represent strong discontinuities which sets it apart from other interface numerical methods.*

4. Constitutive Models for Progressive Debonding and propagating Strong Discontinuity along the Interface

With the variational structure of the edge-stabilized finite-strain interfacial model in hand, we now concentrate on the kinematic models for strong discontinuity or the interfacial damage phenomenon under various loading conditions. These models are based on the notion of irreversible damage evolution and consequently are inspired by the internal variable formalism employed in computational inelasticity literature [36]. We develop evolution equations for the

gap function that model interfacial separation and/or sliding, via Kuhn-Tucker complementary conditions from constrained optimization theory. Specifically, the discrete damage evolution or flow rule for the residual gap ζ and the material softening/hardening parameter $\boldsymbol{Q}$ are derived in a manner analogous to the variational treatment of elastoplasticity as presented in [36,44]. In contrast to cohesive element method [1,15,25,32,44], we use an incremental approach to develop the evolution equation or flow rule for each internal variable [21,41]. Accordingly, the total free energy of the multi-constituent material domain at time $t \in \mathcal{T} =]0,T[$ incorporating both bulk material and interfacial energies can be expressed as:

$$
\mathcal{P}_t\left(\boldsymbol{\phi}_t^{(1)}, \boldsymbol{\phi}_t^{(2)}, \boldsymbol{\zeta}_t, \boldsymbol{Q}_t\right) = \left[\sum_{\alpha=1}^{2} \int_{\Omega^{(\alpha)}} W^{(\alpha)}\left(\boldsymbol{F}_t^{(\alpha)}\right) dV + \mathcal{P}_{ext}\left(\boldsymbol{\phi}_t^{(\alpha)}\right)\right]
$$
$$
- \int_{\Gamma_I} \boldsymbol{\lambda} \cdot \left(\llbracket \boldsymbol{\phi}_t \rrbracket - \boldsymbol{\zeta}_t\right) - \frac{1}{2}\boldsymbol{Q}_t \cdot \boldsymbol{D}^{-1} \cdot \boldsymbol{Q}_t \, dA \tag{28}
$$

where the potential energy of external forces $P_{ext}\left(\boldsymbol{\phi}_t^{(\alpha)}\right)$ contains the contributions from the body forces:

$$
\mathcal{P}_{ext}\left(\boldsymbol{\phi}_t^{(\alpha)}\right) = -\int_{\Omega^{(\alpha)}} \rho_0 \boldsymbol{B}^{(\alpha)} \cdot \boldsymbol{\phi}_t^{(\alpha)} \, dV \tag{29}
$$

The present approach is based on the notion of incremental updating of the nonlinearly evolving internal variables while in our earlier work on interfacial mechanics we had employed a potential function approach with embedded ζ, thereby facilitating the evolution of total ζ at any instant in time. It is to be noted that frictional model incorporated in the present developments for damage in comparison gets activated only due to the tangential component of the interface traction that triggers local shearing and, in the present context of finite deformation framework, local rotational effects. Rotational effects necessitate objective update of the stress and the stress-like quantities which is readily facilitated via the variationally consistent pull-back and push-forward operations embedded in the derivation of these quantities. However, introduction of friction renders the damage evolution flow rule non-associative and therefore requires a rate form for the enforcement of normality condition in the evolution of frictional damage.

Recall the derivation of the expression for the Lagrange multiplier in (18). Substituting (18) into (28), we arrive at an expression for the potential energy for multi-constituent material, accounting for the interfacial energy, however without explicit appearance of the Lagrange multiplier λ:

$$\mathcal{P}_t\left(\boldsymbol{\phi}_t^{(1)},\boldsymbol{\phi}_t^{(2)},\boldsymbol{\zeta}_t,\boldsymbol{Q}_t\right)=\left[\sum_{\alpha=1}^{2}\int_{\Omega^{(\alpha)}}W^{(\alpha)}\left(\boldsymbol{F}^{(1)},\boldsymbol{F}^{(2)}\right)dV+\mathcal{P}_{ext}\left(\boldsymbol{\phi}_t^{(\alpha)}\right)\right]$$
$$-\int_{\Gamma_I}\left(\{\boldsymbol{P}\cdot\boldsymbol{N}\}+\boldsymbol{\tau}_s\cdot\frac{1}{2}\left(\llbracket\boldsymbol{\phi}_t\rrbracket-\boldsymbol{\zeta}\right)\right)\cdot\left(\llbracket\boldsymbol{\phi}_t\rrbracket-\boldsymbol{\zeta}_t\right)-\frac{1}{2}\boldsymbol{Q}_t\cdot\mathbf{D}^{-1}\cdot\boldsymbol{Q}_t\,dA \tag{30}$$

where W is the stored-energy function, $\mathcal{P}_{ext}$ is the external energy function, $\mathbf{D}^{-1}$ is the hardening/softening tangent compliance tensor, and $\boldsymbol{Q}_t$ is the hardening/softening parameter. The last term in (30) appears due to the hardening function $\mathcal{H}$ [36] and for simplicity, we have assumed $\mathcal{H}$ to be quadratic.

Remark. *The potential energy provided in (30) is obtained by substituting the expression of the Lagrange multiplier. An important point to note is that explicit appearance of Lagrange multiplier λ which would have been an additional unknown in the system has been substituted by consistently derived interface coupling terms that eliminate the additional unknown. In addition, equation (30) leads to the stabilized formulation (27) by taking the variational derivative with respect to $\boldsymbol{\phi}^{(1)}$ and $\boldsymbol{\phi}^{(2)}$. Another example of having a potential energy function for elastoplasticity is given in [47].*

Remark. In our previous work [44], we used potential energy based approach along with solving local nonlinear problem to calculate the total residual gap, and this method is being termed as the *total* approach. The *incremental* approach proposed here has several advantages compared to the total approach in [44]. The proposed approach being incrementally objective accommodates friction together with other debonding cases in a unified manner. This results in improved numerical behavior in the finite strain range than the total approach.

As illustrated in [33], taking variational derivative of (30) with respect to the inelastic gap term $\boldsymbol{\zeta}$, we arrive at the interface traction term that is analogous to the term derived in [44] and is defined as:

$$\boldsymbol{T}:=\{\boldsymbol{P}\cdot\boldsymbol{N}\}+\left\|\boldsymbol{\tau}^s\right\|\left(\llbracket\boldsymbol{\phi}\rrbracket-\boldsymbol{\zeta}\right) \tag{31}$$

Note that in the definition of the interface traction term, we use the norm of the stability tensor $\boldsymbol{\tau}^s$ to maintain the direction of the discontinuity term $\left(\llbracket\boldsymbol{\phi}\rrbracket-\boldsymbol{\zeta}\right)$. This is a simplification that enables radial return algorithm for debonding constitutive models that we use in the next section.

Following the ideas from [36], we now use the interface traction (31) to define the damage energy dissipation at time $\xi\in\mathcal{T}$ as:

$$\mathcal{D}_\xi^P := \dot{\zeta}_\xi \cdot \left[\left\{ \boldsymbol{P}\left(\boldsymbol{F}_\xi^{(\alpha)}\right) \boldsymbol{N} \right\} + \|\boldsymbol{\tau}^s\| \left([\![\boldsymbol{\phi}_\xi]\!] - \boldsymbol{\zeta}_\xi \right) \right] - \dot{\boldsymbol{Q}}_\xi \cdot \mathbf{D}^{-1} \cdot \boldsymbol{Q}_\xi \geq 0 \tag{32}$$

where $\left\{ \boldsymbol{\phi}_\xi^{(\alpha)}, \boldsymbol{\zeta}_\xi, \boldsymbol{Q}_\xi \right\}$ must lie within the elastic domain. We emphasize that for any admissible deformation map $\boldsymbol{\phi}_\xi^{(\alpha)}$, the yield surface associated with the yield condition $f\left(\boldsymbol{T}, \boldsymbol{Q}_\xi\right) \leq 0$ is:

$$\mathbb{E} := \left\{ \left(\boldsymbol{T}, \boldsymbol{Q}_\xi\right) \in \left(\mathbb{L}_2\right)^3 \times \mathbb{R}^m \mid f\left(\boldsymbol{T}, \boldsymbol{Q}_\xi\right) \leq 0 \right\} \tag{33}$$

Note that the damage yield condition $f\left(\boldsymbol{T}, \boldsymbol{Q}_\xi\right)$ is a function of both the interface traction $\boldsymbol{T}$ and the hardening/softening parameter $\boldsymbol{Q}_\xi$. We now develop the formulation of total dissipation by combining the damage dissipation $\mathcal{D}_\xi^P$ with the damage yield condition $f\left(\boldsymbol{T}, \boldsymbol{Q}_\xi\right)$. Thus, the total dissipation up to time t can be evaluated by integrating over the entire interface and for the total elapsed time:

$$\mathcal{L}_t^P = \int_0^t \int_{\Gamma_I} \left\{ \mathcal{D}_\xi^P - \gamma_\xi f\left[\left\{ \boldsymbol{P}\left(\boldsymbol{F}_\xi^{(\alpha)}\right) \boldsymbol{N} \right\} + \|\boldsymbol{\tau}^s\| \left([\![\boldsymbol{\phi}_\xi]\!] - \boldsymbol{\zeta}_\xi \right), \boldsymbol{Q}_\xi \right] \right\} dA \, d\xi \tag{34}$$

Here, γ_ξ is considered the damage consistency parameter, which enforces the admissibility constraint (33) at the instant ξ in time and is taken to lie in the positive cone $\mathbb{K}^P$ defined as:

$$\mathbb{K}^P := \left\{ \gamma_\xi \mid \gamma_\xi \in L_2\left(\Gamma_I\right) \right\} \tag{35}$$

Now we consider the time-discrete counterpart of functional (34). Taking $t = t_{n+1} = t_n + \Delta t$ as the current time level, where $t = t_n$ is the previous time level, we can rewrite the time discrete form of (34) along with (32) as follows:

$$\mathcal{L}_{n+1}^P = \mathcal{L}_n^P + \int_{t_n}^{t_{n+1}} \int_{\Gamma_I} \left\{ \dot{\boldsymbol{\zeta}}_\xi \cdot \left[\left\{ \boldsymbol{P}\left(\boldsymbol{F}_\xi^{(\alpha)}\right) \boldsymbol{N} \right\} + \|\boldsymbol{\tau}^s\| \left([\![\boldsymbol{\phi}_\xi]\!] - \boldsymbol{\zeta}_\xi \right) \right] - \dot{\boldsymbol{Q}}_\xi \cdot \mathbf{D}^{-1} \cdot \boldsymbol{Q}_\xi \right\} dA \, d\xi$$
$$- \int_{t_n}^{t_{n+1}} \int_{\Gamma_I} \left\{ \gamma_\xi f\left[\left\{ \boldsymbol{P}\left(\boldsymbol{F}_\xi^{(\alpha)}\right) \boldsymbol{N} \right\} + \|\boldsymbol{\tau}^s\| \left([\![\boldsymbol{\phi}_\xi]\!] - \boldsymbol{\zeta}_\xi \right), \boldsymbol{Q}_\xi \right] \right\} dA \, d\xi \tag{36}$$

The history of the state variables at the interface over the interval $[0, t_n]$ is assumed to be known, while the unknown variables at time t_{n+1} along with the yield function are denoted as:

$$\chi_{n+1} := \left\{ \boldsymbol{\phi}_{n+1}^{(1)}, \boldsymbol{\phi}_{n+1}^{(2)}, \boldsymbol{\zeta}_{n+1}, \boldsymbol{Q}_{n+1}, \Delta\gamma \right\} \tag{37}$$

$$f_{n+1} := f\left[\left\{ \boldsymbol{P}\left(\boldsymbol{F}_{n+1}^{(\alpha)}\right) \boldsymbol{N} \right\} + \|\boldsymbol{\tau}^s\| \left([\![\boldsymbol{\phi}_{n+1}]\!] - \boldsymbol{\zeta}_{n+1} \right), \boldsymbol{Q}_{n+1} \right] \tag{38}$$

Applying the backward Euler difference scheme to (36) results in the following expressions:

$$\mathcal{L}_{n+1}^{P}\left(\boldsymbol{\chi}_{n+1}\right) := \mathcal{L}_{n}^{P} + \int_{\Gamma_{I}} \left\{ \left(\boldsymbol{\zeta}_{n+1} - \boldsymbol{\zeta}_{n}\right) \cdot \left[\left\{ \boldsymbol{P}\left(\boldsymbol{F}_{n+1}\right) \boldsymbol{N} \right\} + \left\| \boldsymbol{\tau}^{s} \right\| \left(\llbracket \boldsymbol{\phi}_{n+1} \rrbracket - \boldsymbol{\zeta}_{n+1} \right) \right] \right\} dA$$
$$- \int_{\Gamma_{I}} \left\{ \Delta\gamma f_{n+1} + \boldsymbol{Q}_{n+1} \cdot \mathbf{D}^{-1} \cdot \left(\boldsymbol{Q}_{n+1} - \boldsymbol{Q}_{n}\right) \right\} dA \tag{39}$$

where $\Delta\gamma := \gamma \Delta t$ is the incremental consistency parameter.

We now return to the potential functional (30) and define a discrete variational form for interface damage as the total free energy available at time t_{n} expressed in terms of the total free energy at time t_{n+1} along with the dissipation during the interval $[t_{n}, t_{n+1}]$:

$$\hat{\mathcal{P}}_{n}\left(\boldsymbol{\chi}_{n+1}\right) := \mathcal{P}_{n+1}\left(\boldsymbol{\chi}_{n+1}\right) + \left(\mathcal{L}_{n+1}^{P}\left(\boldsymbol{\chi}_{n+1}\right) - \mathcal{L}_{n}^{P} \right) \tag{40}$$

Substituting (30) and (39) in (40) and rearranging, we arrive at the following expression wherein all the interface contribution is accumulated in the term $\hat{\mathcal{L}}_{n}\left(\boldsymbol{\chi}_{n+1}\right)$

$$\hat{\mathcal{P}}_{n}\left(\boldsymbol{\chi}_{n+1}\right) := \left[\sum_{\alpha=1}^{2} \int_{\Omega^{(\alpha)}} W^{(\alpha)}\left(\boldsymbol{\phi}_{n+1}^{(\alpha)}, \boldsymbol{\zeta}_{n+1}\right) dV + P_{ext}\left(\boldsymbol{\phi}_{n+1}^{(\alpha)}\right) \right] + \hat{\mathcal{L}}_{n}\left(\boldsymbol{\chi}_{n+1}\right) \tag{41}$$

$$\hat{\mathcal{L}}_{n}\left(\boldsymbol{\chi}_{n+1}\right) = \int_{\Gamma_{I}} \left[\left\{ \boldsymbol{P}\left(\boldsymbol{F}_{n+1}\right) \boldsymbol{N} \right\} + \frac{\left\| \boldsymbol{\tau}^{s} \right\|}{2} \left(\llbracket \boldsymbol{\phi}_{n+1} \rrbracket - \boldsymbol{\zeta}_{n+1} \right) \right] \cdot \left(\llbracket \boldsymbol{\phi}_{n+1} \rrbracket - \boldsymbol{\zeta}_{n+1} \right) dA$$
$$+ \int_{\Gamma_{I}} \left(\boldsymbol{\zeta}_{n+1} - \boldsymbol{\zeta}_{n}\right) \cdot \left[\left\{ \boldsymbol{P}\left(\boldsymbol{F}_{n+1}\right) \boldsymbol{N} \right\} + \left\| \boldsymbol{\tau}^{s} \right\| \left(\llbracket \boldsymbol{\phi}_{n+1} \rrbracket - \boldsymbol{\zeta}_{n+1} \right) \right] dA \tag{42}$$
$$- \int_{\Gamma_{I}} \left\{ \Delta\gamma f_{n+1} + \boldsymbol{Q}_{n+1} \cdot \mathbf{D}^{-1} \cdot \left(\boldsymbol{Q}_{n+1} - \boldsymbol{Q}_{n}\right) \right\} + \frac{1}{2} \boldsymbol{Q}_{n+1} \cdot \mathbf{D}^{-1} \cdot \boldsymbol{Q}_{n+1} dA$$

To show that (41) has an underlying variational structure, the next crucial step is to verify that the stationary conditions of (41) furnish the weak form of the governing equations for interfacial damage. We utilize this weak form in our finite element formulation. Accordingly, we first specify the spaces of trial functions for the fields:

$$\mathcal{S}^{(\alpha)} = \left\{ \boldsymbol{\phi}^{(\alpha)} \middle| \boldsymbol{\phi}^{(\alpha)} \in \left[H^{1}\left(\Omega^{(\alpha)}\right) \right]^{n_{sd}}, \det\left(\boldsymbol{F}^{(\alpha)}\left(\boldsymbol{\phi}^{(\alpha)}\right)\right) > 0, \left. \boldsymbol{\phi}^{(\alpha)} \right|_{\Gamma^{(\alpha)} \backslash \Gamma_{I}} = \boldsymbol{X}^{(\alpha)} \right\} \tag{43}$$

$$\mathcal{X}_{\zeta} = \left\{ \boldsymbol{\zeta} \middle| \boldsymbol{\zeta} \in \left[L_{2}\left(\Gamma_{I}\right) \right]^{n_{sd}} \right\} \tag{44}$$

$$\mathcal{X}_{Q} = \left\{ \boldsymbol{Q} \middle| \boldsymbol{Q} \in \left[L_{2}\left(\Gamma_{I}\right) \right]^{n_{sd}} \right\} \tag{45}$$

Then, taking variational derivative [36] of (41) we obtain the following weak forms of the governing equations:

$$\delta\widehat{\mathcal{P}}_n\left(\boldsymbol{\chi}_{n+1},\boldsymbol{\eta}_0\right)=\sum_{\alpha=1}^{2}\int_{\Omega^{(\alpha)}}\left[\mathrm{GRAD}\,\boldsymbol{\eta}_0^{(\alpha)}:\boldsymbol{P}^{(\alpha)}-\boldsymbol{\eta}_0^{(\alpha)}\cdot\rho_0^{(\alpha)}\boldsymbol{B}^{(\alpha)}\right]\mathrm{dV}$$

$$+\int_{\Gamma_I}\left[\left\{\boldsymbol{P}\cdot\boldsymbol{N}\right\}+\left\|\boldsymbol{\tau}^s\right\|\left(\left[\!\left[\boldsymbol{\phi}_{n+1}\right]\!\right]-\boldsymbol{\zeta}_n\right)-\Delta\gamma\left\|\boldsymbol{\tau}^s\right\|\partial_T f_{n+1}\right]\cdot\left[\!\left[\boldsymbol{\eta}_0\right]\!\right]\mathrm{dA} \quad (46)$$

$$+\int_{\Gamma_I}\left[\left(\left[\!\left[\boldsymbol{\phi}_{n+1}\right]\!\right]-\boldsymbol{\zeta}_n\right)-\Delta\gamma\partial_T f_{n+1}\right]\cdot\left\{\left(\mathrm{GRAD}\,\boldsymbol{\eta}_o:\boldsymbol{A}\right)\cdot\boldsymbol{N}\right\}\mathrm{dA}$$

$$\delta\widehat{\mathcal{P}}_n\left(\boldsymbol{\chi}_{n+1},\boldsymbol{\beta}\right)=\int_{\Gamma_I}\left(\boldsymbol{\zeta}_{n+1}-\boldsymbol{\zeta}_n-\Delta\gamma\partial_T f_{n+1}\right)\cdot\left(-\left\|\boldsymbol{\tau}^s\right\|\boldsymbol{\beta}\right)\mathrm{dA}=0 \quad (47)$$

$$\delta\widehat{\mathcal{P}}_n\left(\boldsymbol{\chi}_{n+1},\boldsymbol{p}\right)=\int_{\Gamma_I}\left[\boldsymbol{D}^{-1}\cdot\left(\boldsymbol{Q}_{n+1}-\boldsymbol{Q}_n\right)+\Delta\gamma\partial_Q f_{n+1}\right]\cdot\left(-\boldsymbol{p}\right)\mathrm{dA}=0 \quad (48)$$

$$\delta\widehat{\mathcal{P}}_n\left(\boldsymbol{\chi}_{n+1},\lambda\right)=\int_{\Gamma_I}\lambda f_{n+1}\,\mathrm{dA}=0 \quad (49)$$

that hold for arbitrary displacement variations $\boldsymbol{\eta}_0\in\mathcal{V}$, residual gap variations $\boldsymbol{\beta}\in\mathcal{X}_\zeta$, hardening variations $\boldsymbol{p}\in\mathcal{X}_Q$, and variations $\lambda\in\mathbb{K}^p$.

We summarize the Euler-Lagrange equations for interfacial damage in Box 1.

Box 1. Euler-Lagrange equations for interfacial damage.

- Equilibrium in the bulk domain, and at the traction boundary:

$$\mathrm{DIV}\,\boldsymbol{P}^{(\alpha)}\left(\boldsymbol{F}^{(\alpha)}\right)+\rho_o^{(\alpha)}\boldsymbol{B}^{(\alpha)}=\boldsymbol{0} \qquad \text{in} \quad \Omega^{(\alpha)},\ \alpha=1,2 \quad (50)$$

- Interface traction equilibrium:

$$\boldsymbol{P}^{(1)}\cdot\boldsymbol{N}^{(1)}+\boldsymbol{P}^{(2)}\cdot\boldsymbol{N}^{(2)}=\boldsymbol{0} \qquad \text{on} \quad \Gamma_I \quad (51)$$

- Interface gap constraint:

$$\left[\!\left[\boldsymbol{\phi}_{n+1}\right]\!\right]-\left(\boldsymbol{\zeta}_n+\Delta\gamma\partial_T f_{n+1}\right)=0 \quad (52)$$

- Interface damage flow rule:

$$\boldsymbol{\zeta}_{n+1}=\boldsymbol{\zeta}_n+\Delta\gamma\partial_T f_{n+1} \quad (53)$$

- Interface hardening law:

$$\boldsymbol{Q}_{n+1}=\boldsymbol{Q}_n+\boldsymbol{D}\Delta\gamma\partial_Q f_{n+1} \quad (54)$$

- Kuhn-Tucker consistency condition:

$$f_{n+1} \leq 0, \qquad \Delta\gamma \geq 0, \qquad f_{n+1}\Delta\gamma = 0 \tag{55}$$

To make the discussion precise we now specify damage yield conditions and softening models to develop traction-gap relations. In Section 5, we specify the evolution of the internal variables by separating the constitutive behavior into two regimes: tension and compression. The tension branch is presented in Section 5.1. For the compression case, only the tangential component of the interface traction contributes to the debonding of the material. Consequently, we further separate compression case into compression damage and compression friction as presented in Section 5.2.

5. Interfacial Constitutive Models and Corresponding Return Mapping Algorithms

In the finite element implementation of constitutive models that are based on internal variable formulism, the equilibrium equation (46) is enforced weakly. However, the constitutive model is considered local and therefore enforced pointwise. Consequently, we strongly enforce the yield condition, damage evolution flow rule, and consistency condition at the Gauss points along the interface wherein the residual gap ζ and hardening variable Q are treated as internal variables and are evolved point-wise from t_n to t_{n+1}. This results in a displacement-driven algorithm that is similar to the strain-driven treatment of computational elastoplasticity problems [36]. Assuming isotropy, we have adopted the classical return mapping approach to solve for $(\phi_{n+1}, \zeta_{n+1}, Q_{n+1})$ in a coupled manner. Details of the return mapping algorithm for the case of both tension and compression are described below.

5.1. The tension model

The yield criterion in tension is defined via the following isotropic linear softening model:

$$f(\boldsymbol{T},Q) = \|\boldsymbol{T}\| - (P_c - Q) \tag{56}$$

where P_c is the critical stress at which debonding initiates, and Q is the softening stress. The relation between the tensile stress and the inelastic gap is shown in Figure 2. The interfacial traction $\boldsymbol{T}$ defined in (31) is as follows:

$$\boldsymbol{T} := \{\boldsymbol{PN}\} + \|\boldsymbol{\tau}^s\|([\![\boldsymbol{\phi}]\!] - \zeta) \tag{57}$$

The flow rule and hardening law under the assumption of isotropy are derived as follows:

$$\dot{\zeta} = \underbrace{\dot{\gamma}\left(\partial f / \partial \boldsymbol{T}\right)}_{\text{Normality}}, \qquad\qquad \dot{Q} = H_c\,\dot{\gamma} \tag{58}$$

where the normality condition $\partial f/\partial \boldsymbol{T} = \boldsymbol{n} = \boldsymbol{T}/\|\boldsymbol{T}\|$ defines the unit vector in the direction of the interface traction, $H_c := P_c/\zeta_c$ is the negative slope of the softening curve shown in Figure 2, and ζ_c is the critical residual gap. From (58), we find that $\dot{\gamma} := \|\dot{\zeta}\|$ which implies $\dot{Q} = H_c\,\dot{\gamma} = \left(P_c/\zeta_c\right)\|\dot{\zeta}\|$, namely that Q increases proportional to the rate of increase in the magnitude of the residual gap. Combining the yield function f with the Kuhn-Tucker form results in the constitutive framework [51].
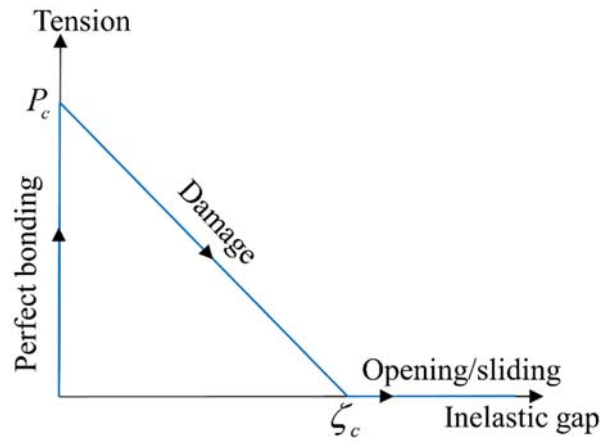
Figure 2. Constitutive behavior in tension.

5.1.1   Return mapping for discontinuity under tensile loading

To develop the return mapping algorithm, let us focus at a Gauss point along the interface Γ_{int}. We assume that the current iterated values of displacements fields in $\Omega^{(1)}$ and $\Omega^{(2)}$, denoted by $\boldsymbol{\phi}_{n+1}^{(i),1}$ and $\boldsymbol{\phi}_{n+1}^{(i),2}$ respectively, are known, along with the previous converged state variables $\left(\boldsymbol{\phi}_n, \zeta_n, Q_n\right)$. The objective is to compute the variables ζ_{n+1} and Q_{n+1} such that the damage yield criterion is satisfied subject to the constraint imposed by the Kuhn-Tucker consistency conditions. Accordingly, we focus on the expression for the interface traction and by plugging in the interface damage flow rule (53), we rewrite the interface traction as:

$$\boldsymbol{T} = \{\boldsymbol{PN}\} + \|\boldsymbol{\tau}^s\|\left(\llbracket \boldsymbol{\phi} \rrbracket - \zeta_{n+1}\right) = \{\boldsymbol{PN}\} + \|\boldsymbol{\tau}^s\|\left(\llbracket \boldsymbol{\phi} \rrbracket - \zeta_n\right) - \|\boldsymbol{\tau}^s\|\Delta\gamma\partial_{\boldsymbol{T}}f_{n+1} \tag{59}$$

From the flow rule evaluated at time t_{n+1} we have:

$$\partial_T f_{n+1} = \frac{\partial \|\boldsymbol{T}_{n+1}\|}{\partial \boldsymbol{T}_{n+1}} = \frac{\boldsymbol{T}_{n+1}}{\|\boldsymbol{T}_{n+1}\|} = \boldsymbol{n}_{n+1} \tag{60}$$

Substituting into (59), we make the following observations on the magnitude and direction of the trial and resultant interface tractions:

$$\|\boldsymbol{T}_{n+1}\| = \|\boldsymbol{T}_{n+1}^{tr}\| - \|\boldsymbol{\tau}^s\| \Delta\gamma \tag{61}$$

where $\boldsymbol{T}_{n+1}^{tr} = \{\boldsymbol{PN}\} + \|\boldsymbol{\tau}^s\|(\llbracket\boldsymbol{\phi}\rrbracket - \boldsymbol{\zeta}_n)$ is based on the last converged value of the gap function. Next, define the trial unit vector $\boldsymbol{n}_{n+1}^{tr}$ in the direction of $\boldsymbol{T}_{n+1}^{tr}$ and trial yield criterion f_{n+1}^{tr} as:

$$\boldsymbol{n}_{n+1}^{tr} = \boldsymbol{n}_{n+1} = \frac{\boldsymbol{T}_{n+1}^{tr}}{\|\boldsymbol{T}_{n+1}^{tr}\|} \tag{62}$$

$$f_{n+1}^{tr} = \|\boldsymbol{T}_{n+1}^{tr}\| - (P_c - Q_n) \tag{63}$$

According to the consistency condition, if $f_{n+1}^{tr} \leq 0$, there is no further damage, namely, $\Delta\gamma = 0$. However, if $f_{n+1}^{tr} > 0$, we can compute $\Delta\gamma$ by satisfying the consistency condition. Substituting Eqn (54), (61) and (63) in (56), we arrive at the equation for $\Delta\gamma$.

$$\begin{aligned} 0 = f_{n+1} &= \|\boldsymbol{T}_{n+1}\| - (P_c - Q_{n+1}) \\ &= \|\boldsymbol{T}_{n+1}^{tr}\| - \|\boldsymbol{\tau}^s\| \Delta\gamma - (P_c - Q_n) + H_c \Delta\gamma \\ &= f_{n+1}^{tr} - (\|\boldsymbol{\tau}^s\| - H_c) \Delta\gamma \end{aligned} \tag{64}$$

Solving (64) for $\Delta\gamma$ yields:

$$\Delta\gamma = \frac{f_{n+1}^{tr}}{(\|\boldsymbol{\tau}^s\| - H_c)} \tag{65}$$

Substituting (65) in (53), (54), and (59), we obtain the updated values for $\boldsymbol{\zeta}_{n+1}$, Q_{n+1} and $\boldsymbol{T}_{n+1}$, respectively. This procedure for updating the internal variables is summarized in Box 2, where $\boldsymbol{x}^{int}$ represents the integration point belonging to the interface segment set $\mathcal{B}$.

Box 2. Return mapping algorithm for damage evolution under tensile loading.

- STEP 1: Database at $x^{\text{int}} \in \mathcal{B}:\ \{\zeta_n, Q_n\}$.

- STEP 2: Given the stress and displacement jump at $x^{\text{int}} \in \mathcal{B}:\ \{\{PN\}, [\![\phi]\!]\}$

- STEP 3: Compute the trial stress and test for inelastic damage evolution

$$T_{n+1}^{tr} = \{PN\} + \|\tau^s\| \left([\![\phi]\!] - \zeta_n \right) \tag{66}$$

$$f_{n+1}^{tr} = \|T_{n+1}^{tr}\| - \left(P_c - Q_n \right) \tag{67}$$

IF $\ f_{n+1}^{tr} \leq 0\ $ THEN

       Elastic step: Set $(\bullet)_{n+1} = (\bullet)_{n+1}^{tr}\ $ & EXIT

ELSE

       Damage evolution step: Proceed to STEP 4.

ENDIF

- STEP 4: Return mapping

$$\Delta\gamma = \frac{f_{n+1}^{tr}}{\left(\|\tau^s\| - H_c \right)} > 0 \tag{68}$$

$$\zeta_{n+1} = \zeta_n + \Delta\gamma n_{n+1} \tag{69}$$

$$Q_{n+1} = Q_n + H_c \Delta\gamma \partial_Q f_{n+1} \tag{70}$$

$$T_{n+1} = T_{n+1}^{tr} - \|\tau^s\| \Delta\gamma n_{n+1} \tag{71}$$

5.2.   Evolution of strong discontinuity under in the compression model

In order to model contact under compression, the residual gap is not permitted to grow in the direction normal to the interface. Consequently, the residual gap $[\![\phi]\!] \cdot N = 0$, where $N = N^{(2)}$ is

the normal vector to the interface. The yield condition is modified as follows:

$$f(\boldsymbol{T}, Q) = \|\boldsymbol{T}_T\| - (P_c - Q) \tag{72}$$

where $\boldsymbol{T}_T = (\boldsymbol{I} - \boldsymbol{N} \otimes \boldsymbol{N})\boldsymbol{T}$ is the shearing traction at the interface. The corresponding flow rules are defied as:

$$\dot{\zeta} = \dot{\gamma}\underbrace{(\partial f / \partial \boldsymbol{T}_T)}_{\text{Normality}}, \qquad\qquad \dot{Q} = H_c\,\dot{\gamma} \tag{73}$$

where $\partial f / \partial \boldsymbol{T}_T = \boldsymbol{n}_T = \boldsymbol{T}_T / \|\boldsymbol{T}_T\|$. When debonding occurs under compressive loading, the effects of friction have been found to be significant [1]. Therefore, we enhance the yield model by incorporating a yield condition for friction that takes the form [37,51]:

$$f(\boldsymbol{T}) = \|\boldsymbol{T}_T\| + \mu_f T_N \tag{74}$$

where $T_N = \boldsymbol{T} \cdot \boldsymbol{N}$ is the contact pressure (positive in tension) and μ_f is the coefficient of friction.

One can combine (72) and (74) into a comprehensive model by employing ideas from multi-surface plasticity [36]. Following the computational inelasticity literature, we determine the damage/softening or friction criteria that is active, by selecting the one that leads to the smallest change in ζ for the given or the current level of traction. Detailed return mapping algorithm for the compression loading case is given in Box 3.

Remark. The flow rule (73) is non-associative when combined with the friction yield condition (74) because slip is only allowed in the tangential direction. However, in the present work we employ a return mapping strategy that serves as a predictor/corrector algorithm which is widely used in the theory of plasticity [36,37].

5.2.1   Return mapping for frictional constraint under compressive loading

In compressive loading, the normal traction does not play any role in damage evolution or in sliding, and therefore shearing traction is the only component that needs to be considered. In this section we only provide the algorithmic treatment for the friction part of compressive loading since the damage in compression is form identical to that in the tension case.

Employing interfacial traction as in (59) and considering only the shearing traction component, the definitions for the trial quantities and the consistency parameter are summarized in Box 3.

Box 3. Return mapping algorithm for friction under compressive loading.

- STEP 1: Database at $x^{int} \in \mathcal{B}$: $\{\zeta_n, Q_n\}$.

- STEP 2: Given the stress and displacement jump at $x^{int} \in \mathcal{B}$: $\{\{PN\}, [\![\phi]\!]\}$

- STEP 3: Compute the trial stress and test for damage evolution

$$T^{tr}_{T,n+1} = (I - N \otimes N)\left[\{PN\} + \|\tau^s\|\left([\![\phi]\!] - \zeta_n\right)\right] \tag{75}$$

$$T_{N,n+1} = N \cdot \left[\{PN\} + \|\tau^s\|[\![\phi]\!]\right] \tag{76}$$

$$f^{tr,\mu_f}_{n+1} = \left\|T^{tr}_{T,n+1}\right\| + \mu_f T_{N,n+1} \tag{77}$$

$$f^{tr,P_c}_{n+1} = \left\|T^{tr}_{T,n+1}\right\| - (P_c - Q) \tag{78}$$

IF $f^{tr}_{n+1} \leq 0$ THEN

   Elastic step: Set $(\bullet)_{n+1} = (\bullet)^{tr}_{n+1}$ & EXIT

ELSE

   Damage evolution step: Proceed to STEP 4.

ENDIF

- STEP 4: Return mapping

   Calculate incremental consistency parameter $\Delta\gamma$

$$\Delta\gamma = \frac{f^{tr,\mu_f}_{n+1}}{\|\tau^s\|} > 0 \tag{79}$$

$$\Delta\gamma = \frac{f^{tr,P_c}_{n+1}}{\left(\|\tau^s\| - H_c\right)} > 0 \tag{80}$$

   Compare (79) and (80), and select the smaller $\Delta\gamma$ and plug into (81):

$$\zeta_{n+1} = \zeta_n + \Delta\gamma\chi_{n+1} \tag{81}$$

$$Q_{n+1} = Q_n + H_c\Delta\gamma\partial_Q f_{n+1} \tag{82}$$

$$\boldsymbol{T}_{T,n+1} = \boldsymbol{T}_{T,n+1}^{tr} - \left\|\boldsymbol{\tau}^s\right\|\Delta\gamma\boldsymbol{n}_{n+1} \tag{83}$$

6. Consistent Linearization

Due to the nonlinear interface constitutive models, we need to solve the weak form (27) in an iterative fashion using the Newton-Raphson algorithm. The linearization of the bulk material terms and the standard DG terms is given in [42]. In the following we primarily focus on the linearization of the term related to the interface damage part.

$$
\begin{aligned}
K_{\text{damage}}\left(\boldsymbol{\eta}_o^{(\alpha)}, \boldsymbol{\phi}^{(\alpha)}, \boldsymbol{\zeta}\right) &= -\int_{\Gamma_I}\left[\left\{(\text{GRAD }\boldsymbol{\eta}_o:\mathbf{A})\cdot\boldsymbol{N}\right\} + [\![\boldsymbol{\eta}_o]\!]\cdot\|\boldsymbol{\tau}_s\|\right]\cdot\left(\frac{\partial}{\partial u}\Delta\gamma\partial_T f_{n+1}\cdot\Delta\boldsymbol{u}\right)dA \\
&= -\int_{\Gamma_I}\tilde{\boldsymbol{T}}(\boldsymbol{\eta}_o)\cdot\left[\frac{\partial}{\partial\boldsymbol{T}}(\Delta\gamma\boldsymbol{n})\cdot\tilde{\boldsymbol{T}}(\Delta\boldsymbol{u})\right]dA
\end{aligned}
\tag{84}
$$

where $\tilde{\boldsymbol{T}}(\cdot) = \left[\left\{(\text{GRAD }(\cdot):\mathbf{A})\cdot\boldsymbol{N}\right\} + [\![\cdot]\!]\cdot\|\boldsymbol{\tau}_s\|\right]$ is the numerical interface flux. The discussion for the linearized tensor expression $\frac{\partial}{\partial\boldsymbol{T}}(\Delta\gamma\boldsymbol{n}) = \frac{\partial\Delta\gamma}{\partial\boldsymbol{T}}\otimes\boldsymbol{n} + \gamma\frac{\partial\boldsymbol{n}}{\partial\boldsymbol{T}}$, which depends on different interfacial constitutive models is presented in Appendix. Along with the standard DG linearization terms presented in [42], the final tangent stiffness matrix is shown as follows:

$$
\begin{aligned}
K\left(\boldsymbol{\eta}_o^{(\alpha)}, \Delta\boldsymbol{u}^{(\alpha)}; \boldsymbol{\phi}^{(\alpha)}\right) &= \sum_{\alpha=1}^{2}\int_{\Omega^{(\alpha)}}\text{GRAD }\boldsymbol{\eta}_o^{(\alpha)}:\mathbf{A}^{(\alpha)}:\text{GRAD }\Delta\boldsymbol{u}^{(\alpha)}\ dV \\
&+ \int_{\Gamma_I}[\![\boldsymbol{\eta}_o]\!]\cdot\boldsymbol{\tau}_s\cdot[\![\Delta\boldsymbol{u}]\!]\ dA + \int_{\Gamma_I}[\![\boldsymbol{\eta}_o]\!]\cdot\left\{(\mathbf{A}:\text{GRAD }\Delta\boldsymbol{u})\cdot\boldsymbol{N}\right\}\ dA \\
&+ \int_{\Gamma_I}\left\{(\text{GRAD }\boldsymbol{\eta}_o:\mathbf{A})\cdot\boldsymbol{N}\right\}\cdot[\![\Delta\boldsymbol{u}]\!]\ dA \\
&+ \int_{\Gamma_I}\left\{(\text{GRAD }\boldsymbol{\eta}_o:\boldsymbol{\Xi}:\text{GRAD }\Delta\boldsymbol{u})\cdot\boldsymbol{N}\right\}\cdot\left([\![([\![\boldsymbol{\phi}]\!]-\zeta_n)-\Delta\gamma\boldsymbol{n}]\!]\right)\ dA \\
&- \int_{\Gamma_I}\tilde{\boldsymbol{T}}(\boldsymbol{\eta}_o)\cdot\left[\frac{\partial}{\partial\boldsymbol{T}}(\Delta\gamma\boldsymbol{n})\cdot\tilde{\boldsymbol{T}}(\Delta\boldsymbol{u})\right]dA
\end{aligned}
\tag{85}
$$

The first four terms on the right hand side of (85) constitute the linearized form of the standard interface DG method present in [42]. The last two terms are related to the residual gap ζ.

Comparing (85) with our previous work in [44], the structural form of the last term is similar. However, the key difference is that we use return mapping algorithm to calculate the incremental value of ζ at integration points as given in Box 2 and 3.

Remark. The tangent stiffness matrix (85) remains symmetric if the loading scenarios only induce tensile and/or compressive debondings. For compressive frictional case, it is not symmetric thereby necessitating an incrementally imposed normality $\left(\partial f / \partial T_T \right)$ condition in the yield function $f\left(T, Q \right)$.

7.   Numerical Results

This section investigates the performance of the proposed interface method across a range of deformation modes. We have employed standard linear Lagrange polynomials and two and three-dimensional test problems are considered. All integral expressions over surfaces and volumes are evaluated using quadrature rules of sufficiently high order. A common neo-Hookean material model is employed, and the strain energy density function is given as follows:

$$W\left(F \right) = \frac{1}{2}\mu\left(\mathrm{tr}\left(F^T F \right) - 3 \right) - \mu \ln J + \frac{1}{2}\lambda\left(J - 1 \right)^2 \tag{86}$$

We first present results for test cases wherein continuity is weakly enforced at specific bi-material interfaces with the gap ζ and this corresponds to the formulation derived in Sections 2 and 3. The treatment of the evolution for ζ is discussed in Sections 4 and 5.

Remark. In the numerical tests presented below, we indicate the interfaces across which the weakly imposed continuity conditions are imposed. For discussion on the algorithmic treatment of generating interfaces within finite element meshes, reader is referred to [48].

7.1.   Patch Tests

7.1.1   Interfacial debonding under tension

We begin with a simple patch test to verify variational consistency of the interface damage formulation. Two blocks of $1 \ \mathrm{mm}^3$ modeled via one brick element each are separated by an interface along which the proposed stabilized interface method is employed, as shown in Figure 3. The material properties used in the neo-Hookean model (86) are $E = 5 \ \mathrm{GPa}$ and $\nu = 0.25$. Prescribed tip displacement $\delta = 0.4 \ \mathrm{mm}$ is applied at all the nodes at the right surface of the domain. Boundary conditions applied on to the left face create a state of uniform tensile stress throughout the domain. Symmetric roller boundary condition is applied on the top surface to prevent rigid body motion. For the evolution of damage, we set the critical stress $P_c = 100 \ \mathrm{MPa}$ and critical inelastic gap $\zeta_c = 0.2 \ \mathrm{mm}$.
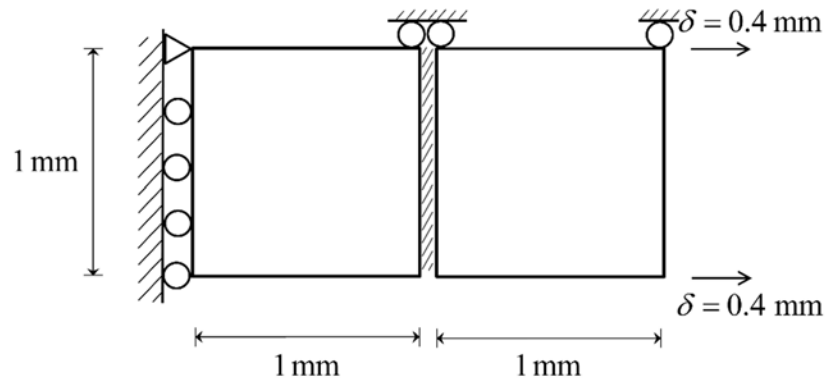
Figure 3. Description of the patch test problem.

The relation between the tension at the right surface and the opening at the interface is shown in Figure 4, which matches exactly the behavior shown in Figure 2 for the softening response. As the magnitude of the applied displacement at the right end is increased, the induced traction increases up to the critical stress $P_c = 100$ MPa and at that point the interfacial debonding gets activated, giving rise to a softening response under progressive debonding.
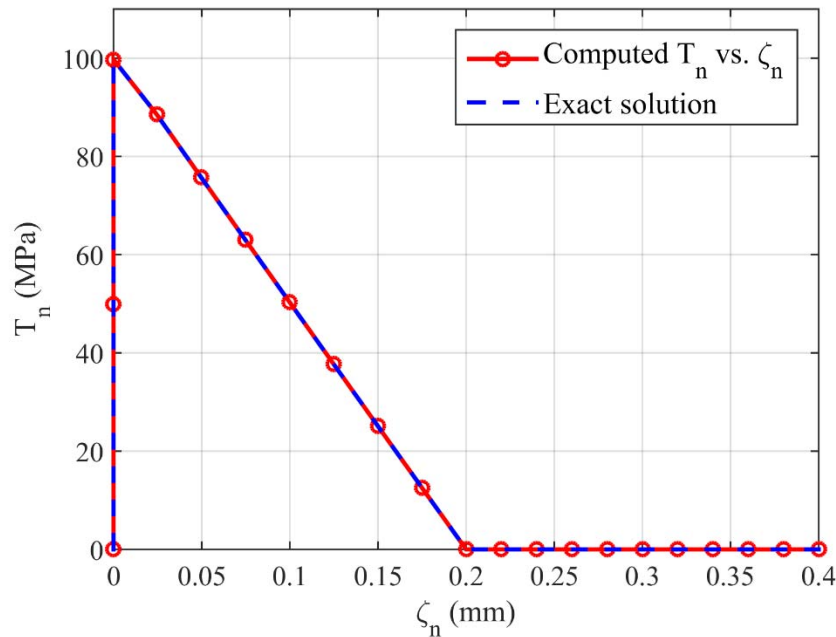
Figure 4. Traction-gap relation between induced traction T_n and the residual gap ζ_n.

Figure 5 represents contour plots of the axial stress for various load levels that is overlaid on the corresponding deformed configurations. Because of isotropic material properties and due to

the applied BCs that produce uniform axial deformation, the axial stress field is constant over the domain. In Figure 5(a), the stress in the elements has not yet reached the critical stress, thus the two blocks are perfectly bonded together. In Figure 5(b), the displacement gap at the interface is significant enough to be noticed for this large deformation test, and the traction is smaller as compared to that in Figure 5(a) due to the damage softening effects. Once the gap between these two blocks exceeds the critical inelastic gap ζ_c, which is shown in Figure 5(c), the two blocks are independent and no longer interact with each other. At this stage the two blocks are completely unloaded and there is no traction between them.

(a)   (b)

(c)
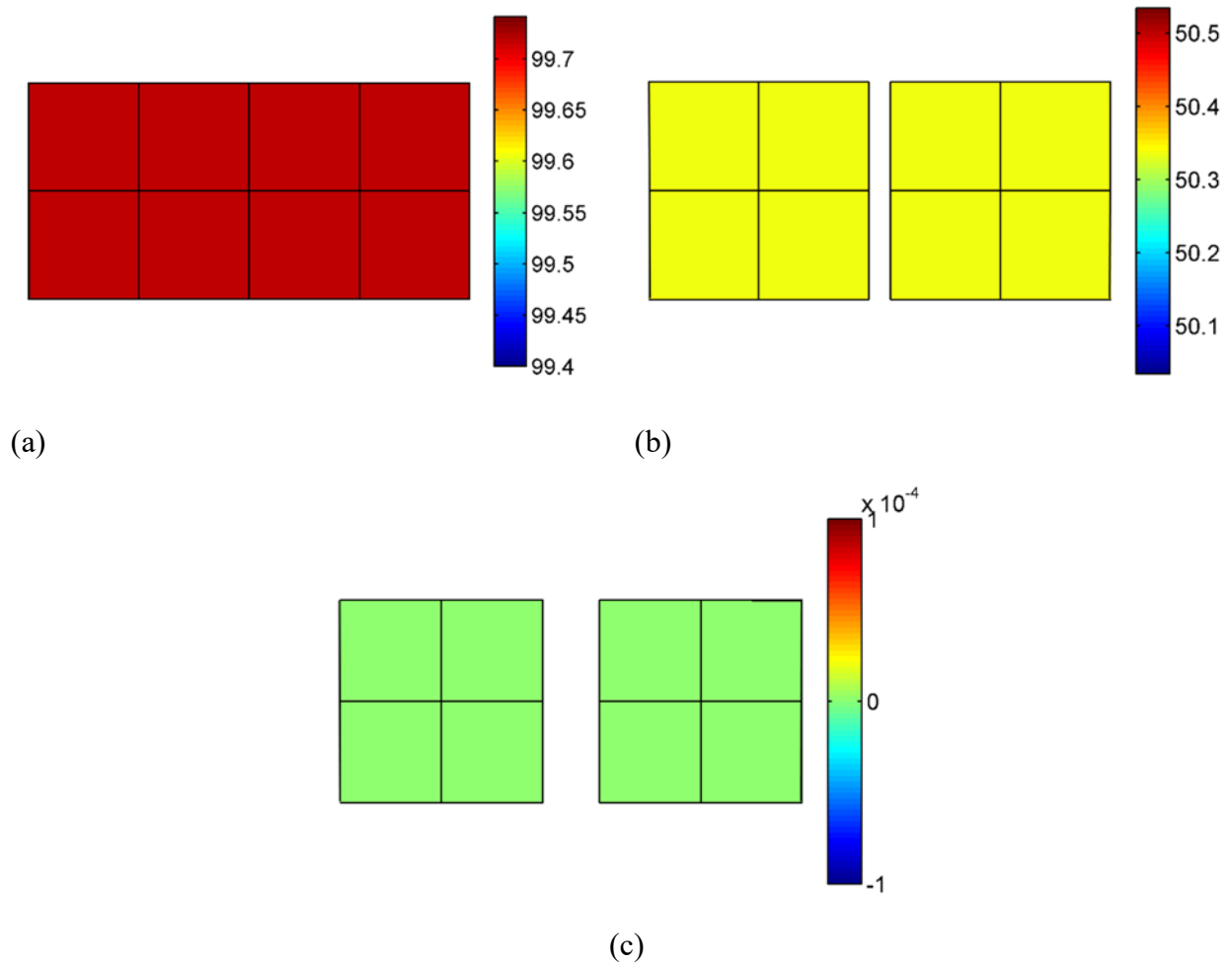
Figure 5. Contour plots of the traction T_n at three different steps: (a) $\zeta = 0\,\text{mm}$;(b) $\zeta = 0.0998\,\text{mm}$; (c) $\zeta = 0.26\,\text{mm}$.

Table 1 presents the Euclidean norm of the out-of-balance force vector computed at each iteration during the Newton-Raphson solution procedure in step 6 when $\zeta = 0.0747\,\text{mm}$. The

observed quadratic rate of convergence numerically confirms consistent linearization and the derivation of the consistent tangent presented in Section 6.

Table 1. Evolution of residual l^2 norm for the patch test.

Iteration Number	Residual Norm
1	2.8833671×10^{1}
2	2.9488081×10^{-1}
3	2.5465645×10^{-5}
4	$7.6179649 \times 10^{-13}$

7.1.2   Debonding under compressive shear

The second patch test is comprised of two blocks with an inclined interface as shown in Figure 6. The material properties are same as in the previous section, with the prescribed displacement $\delta = -0.2$ mm applied at all the nodes at the right surface to induce a compression load on the right block.
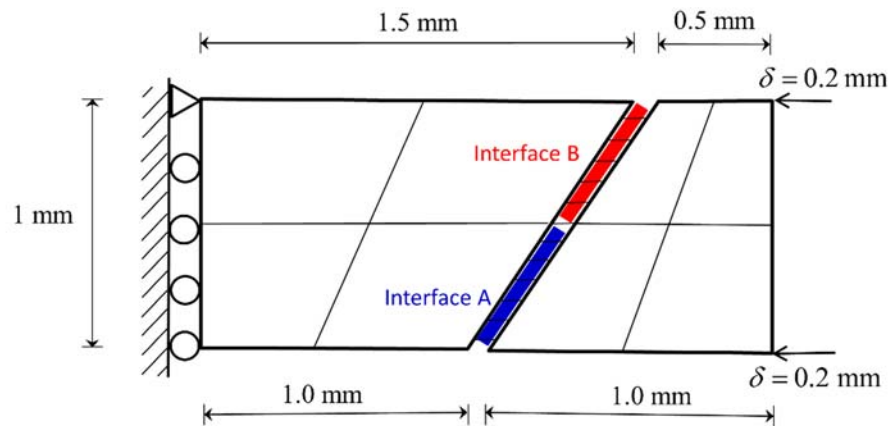
Figure 6. Geometry for patch test with inclined interface.

Figure 7 shows the axial stress contour plots for three load steps. At the inclined interface, the tangential component of traction increases up to the critical value due to the applied compressive displacement as shown in Figure 7(a) and thereafter triggers the compression damage process which leads to the sliding of the right block as shown in Figure 7(b). At the final step, the right block slides down after the tangential shear overcomes the frictional resistance and the stress reduces to zero as shown in Figure 7(c).

27

(a)   (b)

(c)
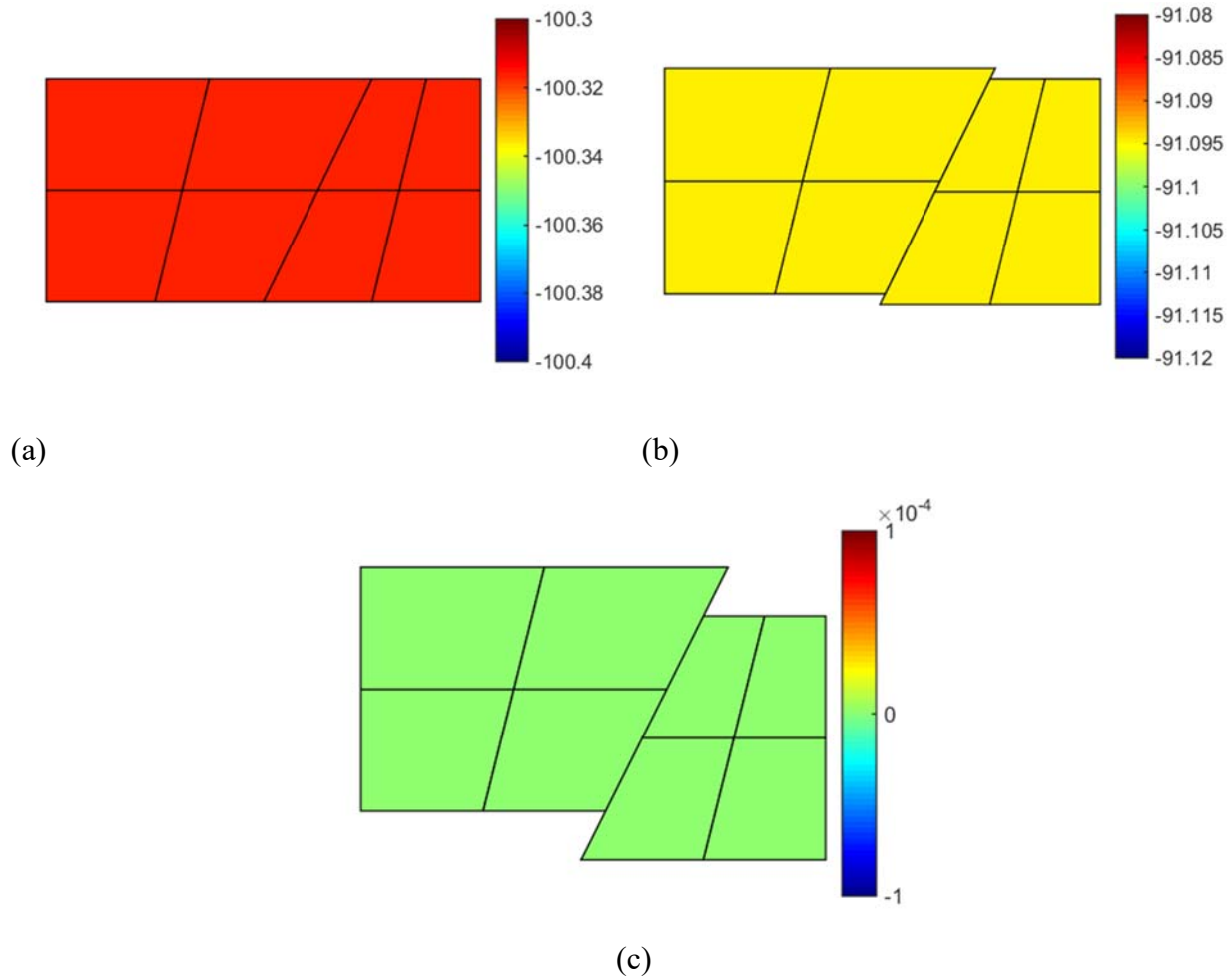
Figure 7. Contour plot of the axial stress σ_{xx} at three different steps: (a) $d = -0.08\,\text{mm}$; (b) $d = -0.12\,\text{mm}$; (c) $d = -0.2\,\text{mm}$.

Table 2. Stability parameter $\left\lVert \boldsymbol{\tau}_s \right\rVert$ for different load steps.

Load step	Interface A	Interface B
1	1.3182×10^5	1.2769×10^5
2	1.3207×10^5	1.2801×10^5
3	1.3234×10^5	1.2836×10^5
4	1.3229×10^5	1.2829×10^5
5	1.3182×10^5	1.2769×10^5

Table 2 shows the evolution of the stability parameter $\|\tau_s\|$ for different load steps. The stability value drops for both interfaces at last step because of switching from compression damage branch to the friction branch. Since the derived τ_s embeds the concepts of area averaging and stress averaging, due to the difference in the element size, the computed values show slight variability that is however within 1%, thus validating the consistent derivation of this stability parameter as a function of the evolving geometric and material nonlinearity.

7.2.   Fiber matrix debonding under transverse loading

This test case is for fiber-matrix debonding under transverse axial loading. The bulk material parameters for the fiber and matrix are: $E_f = 40\,\text{GPa}$, $v_f = 0.4$ and $E_m = 10\,\text{GPa}$, $v_m = 0.33$, respectively. As shown in [17], due to the damage at the interface, there is stress concentration in the matrix near the interface. Therefore we assume that debonding, once initiated at the fiber-matrix interface, can trigger failure inside the matrix as well. Conversely, material failure via fracture can also get initiated in the matrix which can then trigger bimaterial debonding. Since the fiber is invariably much stronger than the matrix material, it is assumed that fiber remains intact during damage evolution. In addition, crack in the matrix is assumed to propagate along the element edges, and in the current implementation, crack propagation through the elements is not considered [30].

The interface properties for debonding are as follows: critical stress $P_c^f = 10\,\text{MPa}$ for fiber-matrix interfaces, and $P_c^m = 30\,\text{MPa}$ for inter-element debonding within the matrix. The critical inelastic gap $\zeta_c = 0.2\,\text{mm}$. Boundary conditions are shown in Figure 8(a); plane strain conditions are applied for the z direction. We apply a displacement increment $\bar{u} = 10^{-4}\,\text{mm}$ at both left and right surfaces at each step. The cross section of the unstructured mesh that is comprised of brick elements is shown in Figure 8(b),
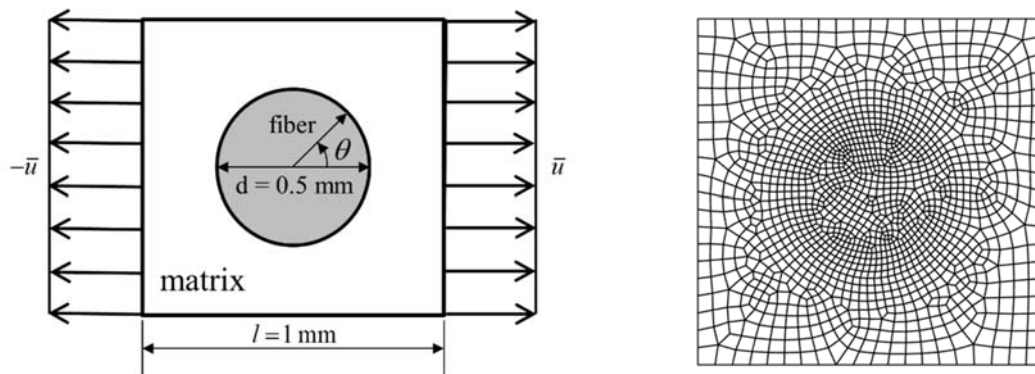
Figure 8. Fiber-matrix debonding problem: a) Problem description; b) Hexahedral element mesh.

Figure 9 shows stress versus strain plot in the direction of the applied loading. The stress is obtained by summing up stresses from all the elements within edges coincident with the left and right surfaces. Since only small deformations are induced, engineering strain is chosen for expressing the results, which is evaluated as the displacement divided by the original length. One can see the four critical stages as a function of the evolution of interfacial debonding and matrix cracking. The contour plots corresponding to these four stages are shown in Figure 10 where displacement field is magnified twenty times to clearly show the process of debonding. The fracture process starts from a state of perfectly bonded fiber and matrix interface and debonding initiates when interfacial stress reaches the critical stress level as shown in Figure 10(a). Then through stage 2 to stage 3, the cracks start to kink into the matrix and grow orthogonal to the direction of principal stress until they reach the edges as shown in Figure 10(b) and Figure 10(c). Finally, multiple cracks initiate inside the matrix that triggers failure of the material as illustrated in Figure 10(d). The overall behavior is consistent with the response reported in [30].
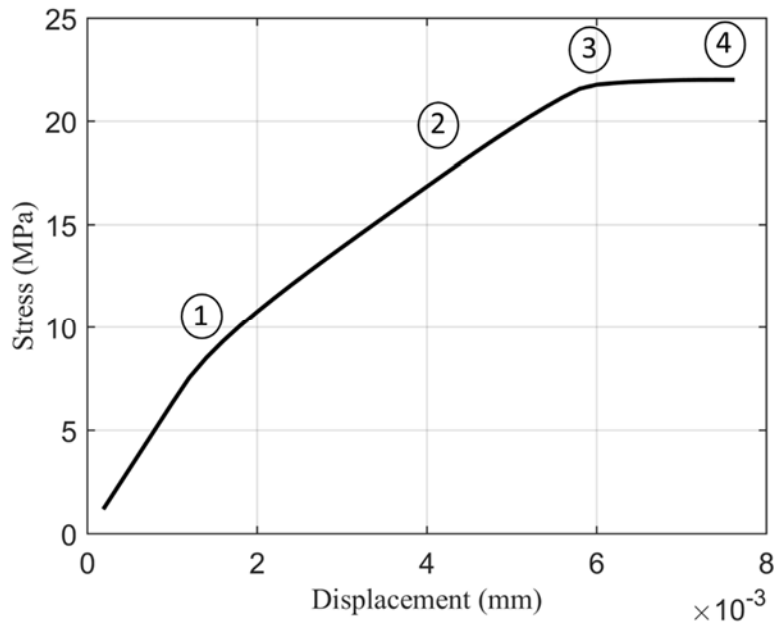
Figure 9. Force-displacement curve for the various stages of the material interface evolution.
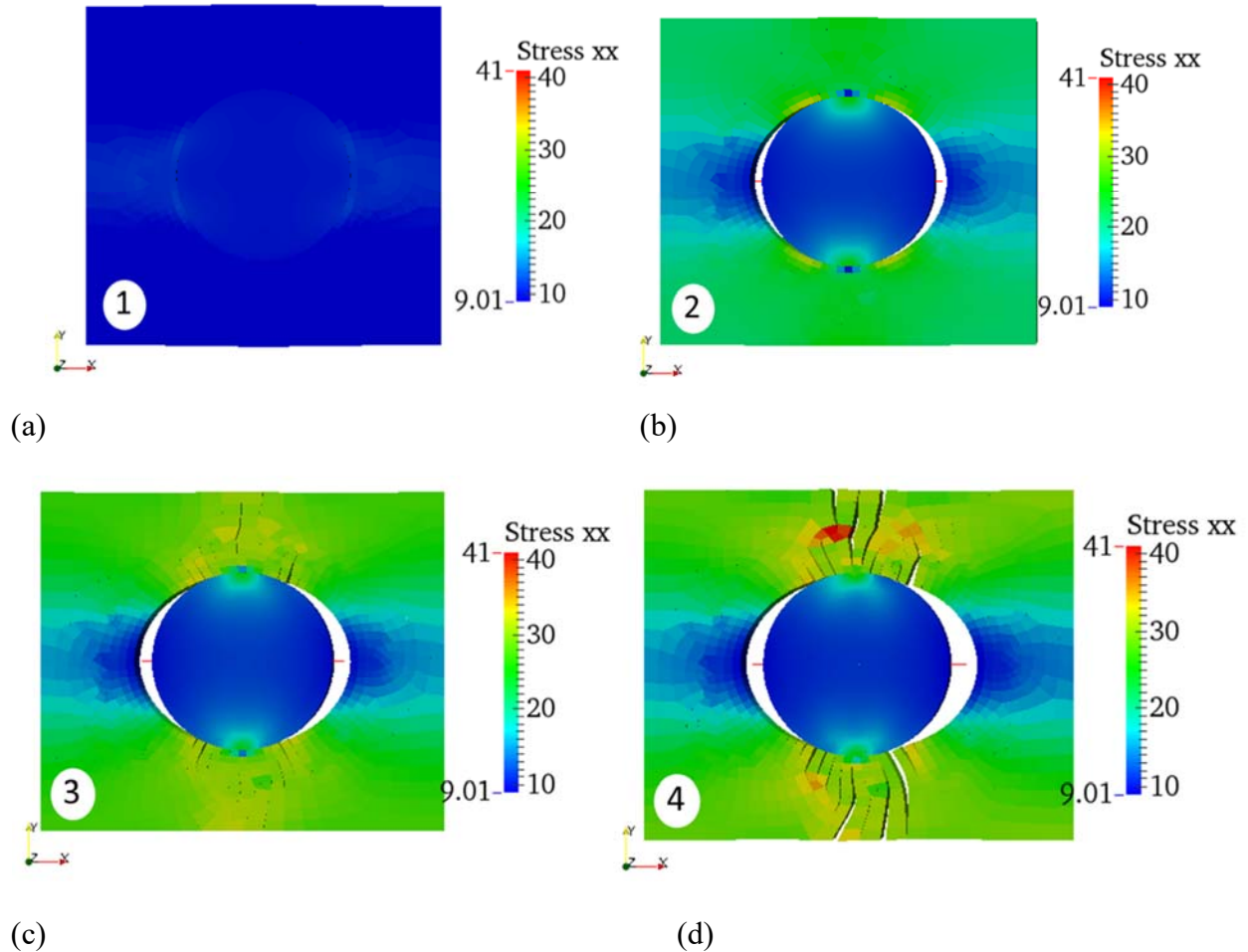
Figure 10. Contour plots of the stress σ_{xx} at four different stages: (a) Initiation of fiber-matrix interfacial debonding; (b) Crack kinking into the matrix; (c) Crack propagation orthogonal to the principal stresses; (d) Multiple cracking and material failure.

Figure 11 shows the plot of the normal component of the displacement gap at interface between the fiber and the matrix. The angle θ is measured as shown in Figure 8(a). A comparison of stress versus applied displacement plot with results presented in Nguyen [30] is shown in Figure 12, and a good comparison during the four steps of the evolution of the problem is attained.
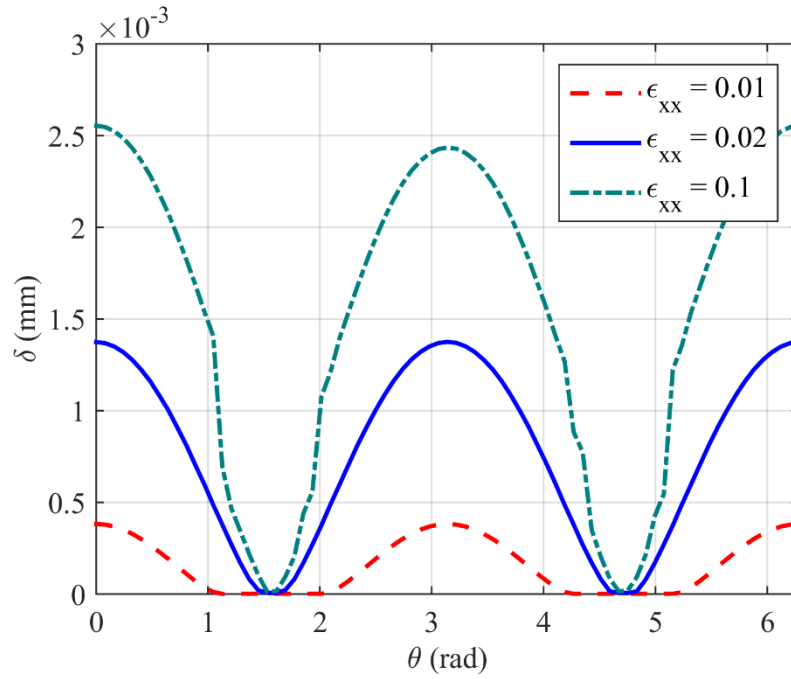
Figure 11. Normal gap between fiber and matrix around the interface.
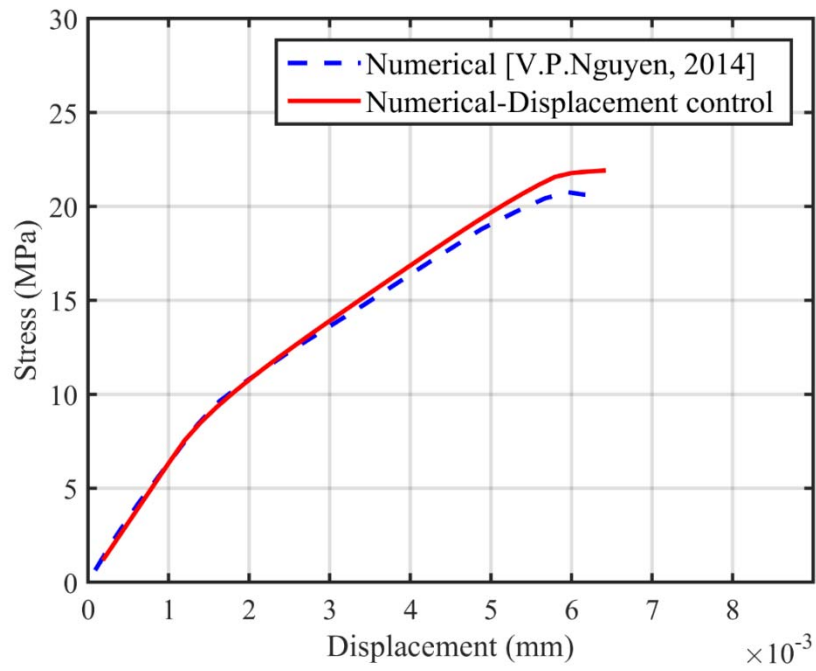
Figure 12. Stress vs. applied displacement plot.

7.3.   Tearing of bimaterial interfaces

This test case presents tearing of bimaterial interface between a soft and a hard material. This problem is inspired by the stretching of a cracked plate in finite elasticity [38, 24], and due to large difference in mechanical material properties it serves as a model problem for tearing of tendons from the bone under excessive mechanical stresses. In this test case, the two plates have an existing partial crack along the interface. Spatial dimensions and boundary conditions are shown in Figure 13. The bottom plate that is comprised of the softer material has same dimensions as in [24] and the proposed interface formulation is employed along the bimaterial interface between the hard and soft material. A given displacement field is applied at the bottom surface of the lower plate that produces 100% strains as shown in Figure 13.

(a)   (b)
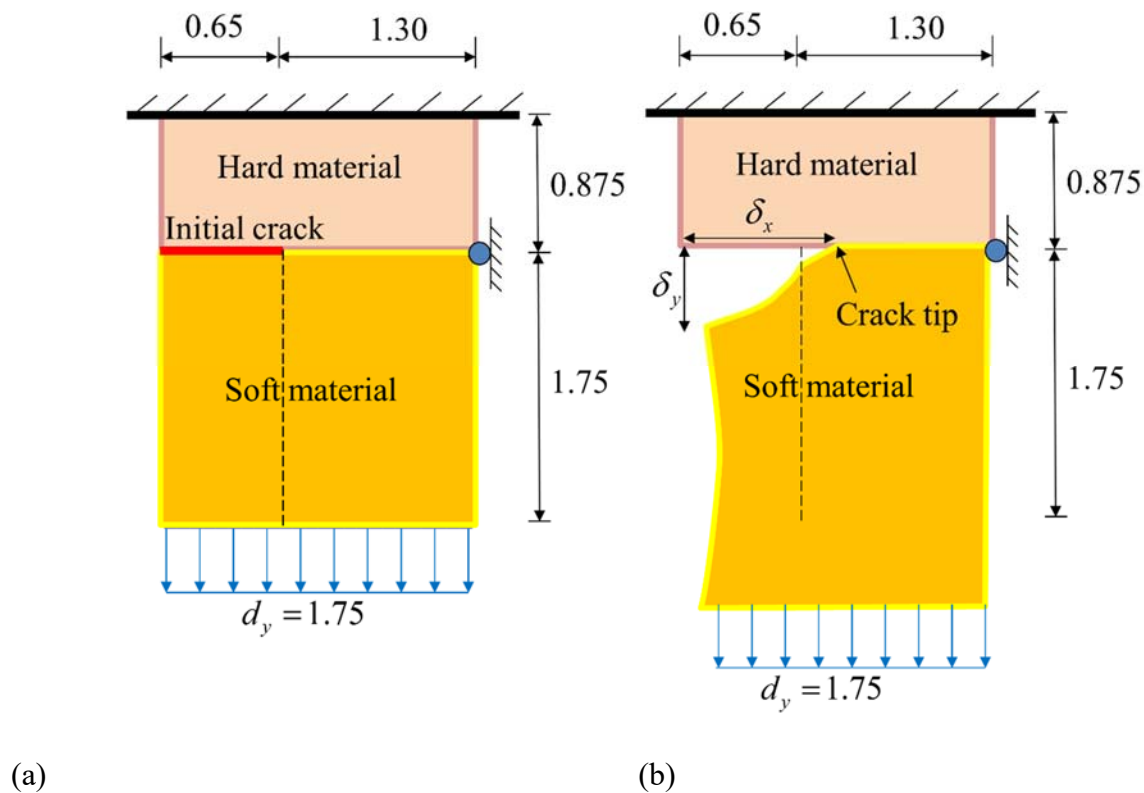
Figure 13. Tearing along soft and hard material interface: (a) original state; (b) deformed state.

We have employed two different material types to study the effects of the material on interfacial debonding evolution: (a) the standard Neo-Hookean material as in (86) for both the plates, and (b) Ogden-type material in (87)-(88) for the bottom plate. In the latter case the top plate is still modeled with the Neo-Hookean material.

The material properties are listed in Table 3. Young's modulus for the top plate is four times larger than that for the bottom plate to simulate the stiff and soft material response. We have employed three meshes with successive refinements to test the robustness of the method. For the

coarse discretization, mesh size is 24×20 for the bottom plate, while for the top plate the mesh discretization is 24×10. For the medium mesh, discretization size is 48×40 for the bottom plate and 48×20 for the top plate. For the fine mesh, discretization is 96×80 for the bottom plate and 96×20 for the top plate. We want to point out that the objective in this problem is to test the stability of the numerical method for coarse meshes, and we note that this solution may not accurately resolve the crack tip stresses and the crack velocity.

Table 3. Coefficients for the two materials.

Neo-Hookean Material			
Top plate	Properties	Bottom plate	Properties
$E_m \, (\text{N/mm}^2)$	16000	$E_f \, (\text{N/mm}^2)$	4000
υ_m	0.44	υ_f	0.44
Damage properties	$P_c \, (\text{MPa})$	$\zeta_c \, (\text{mm})$	
	200	0.2	
Ogden-type Material	Bottom plate		
$c_\alpha \, / \, m_\alpha$	6.3	0.012	−0.010
m_α	1.3	5.0	−2.0
Damage properties	$P_c \, (\text{MPa})$	$\zeta_c \, (\text{mm})$	
	20	0.2	

In Figure 14 and Figure 15, we plot the contours of σ_{yy} at different steps during the evolution of the problem for different mesh refinements. These figures exhibit the process of tearing of the soft material from the hard material, where the problem is run with an applied displacement at the bottom. The pattern of the tearing process for coarse and fine mesh is almost identical, which numerically verifies the robustness of the proposed method. For plotting purpose the range of stress is kept the same in order to obtain an objective comparison between the various frames. Figure 14(a) shows initiation of the tearing process at around 4% applied strain. Figure 14(b) shows stress concentration at the crack tip at 10% strain. The process of tearing along bimaterial interface evolves with an increase in applied strain and finally the two plates are almost

separated as shown in Figure 14(d). We can also see that there is jump in the value of stress across the interface, while the stress is continuous within each of the two subdomains.
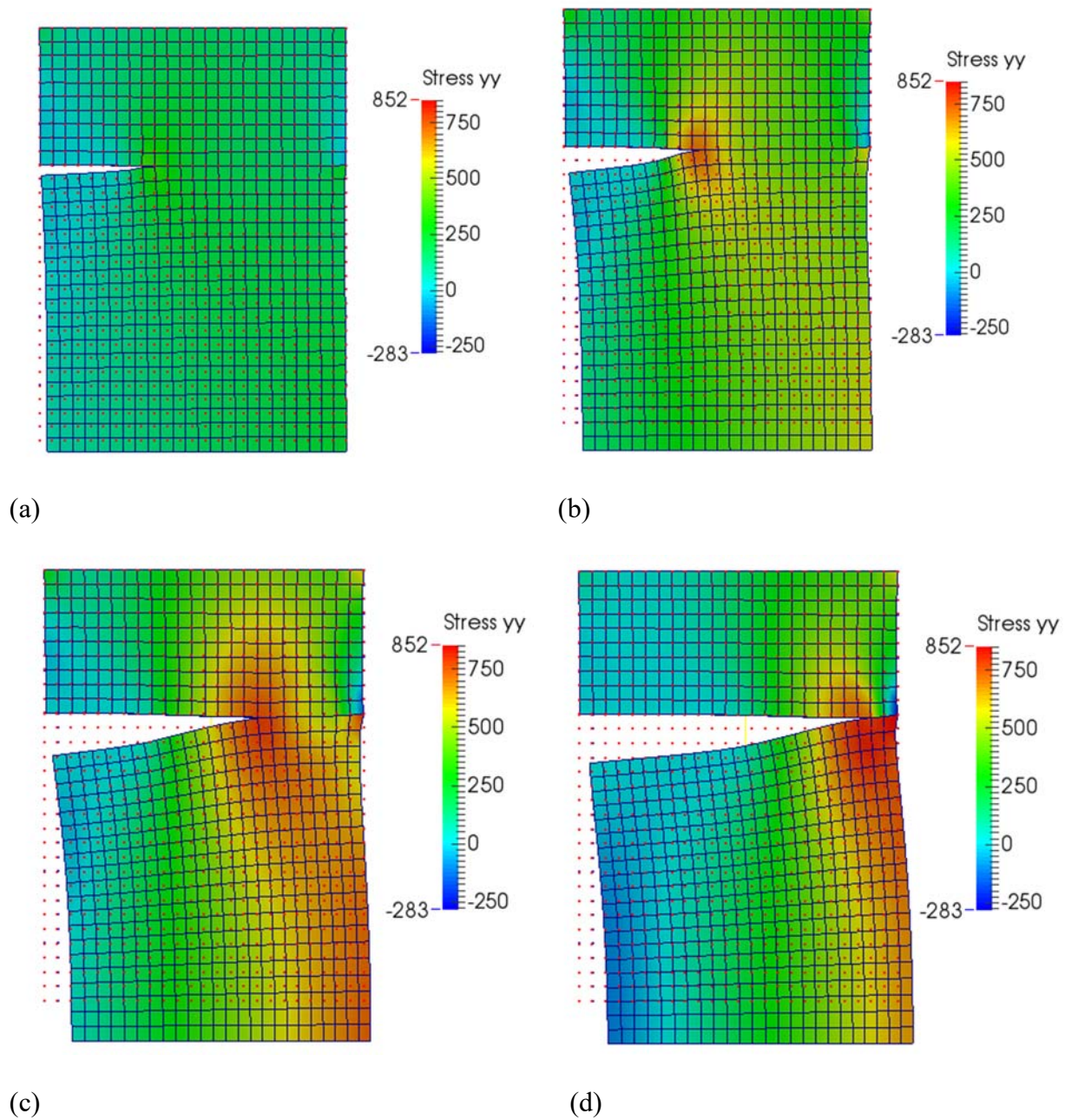

(a)   (b)
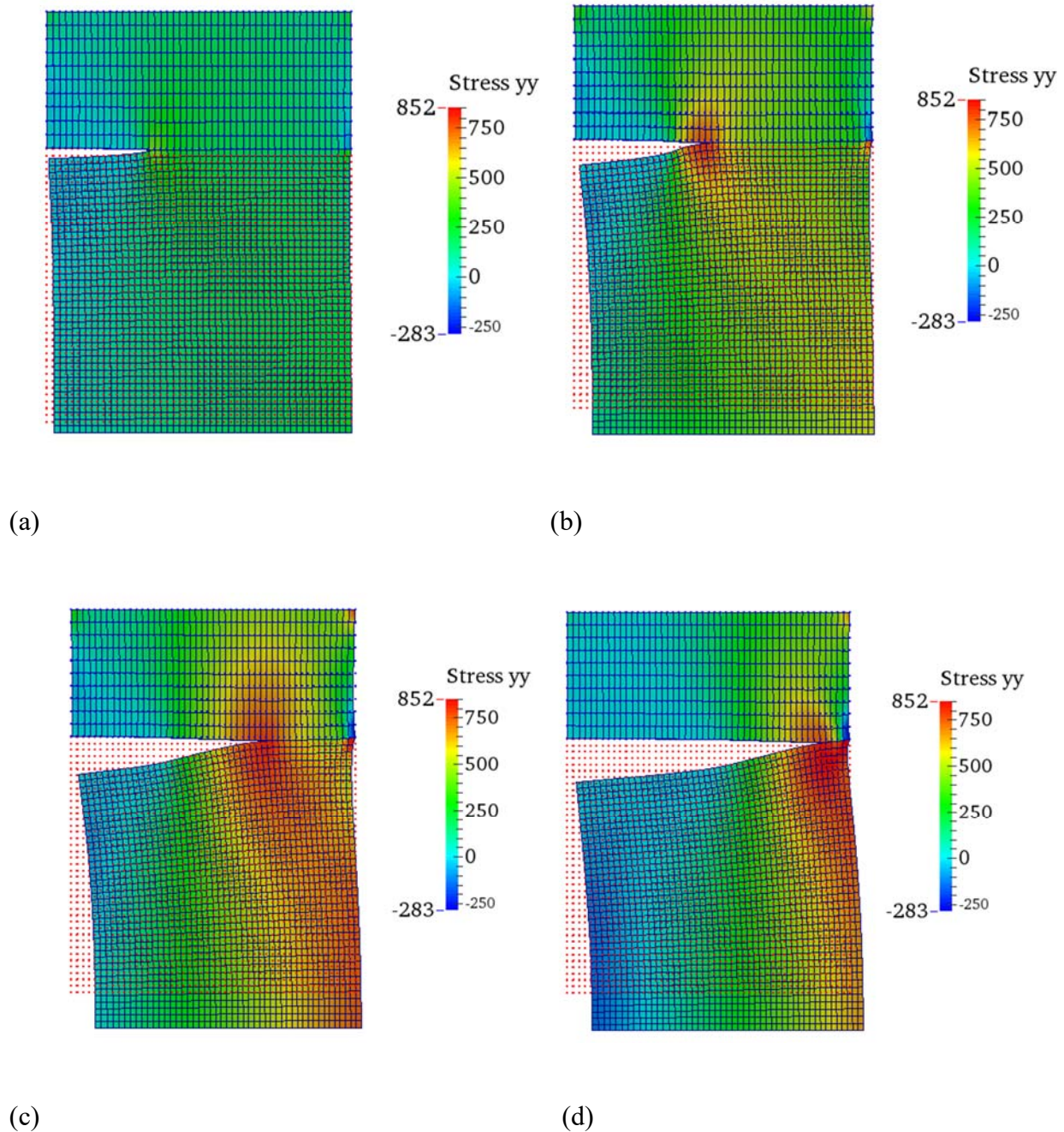

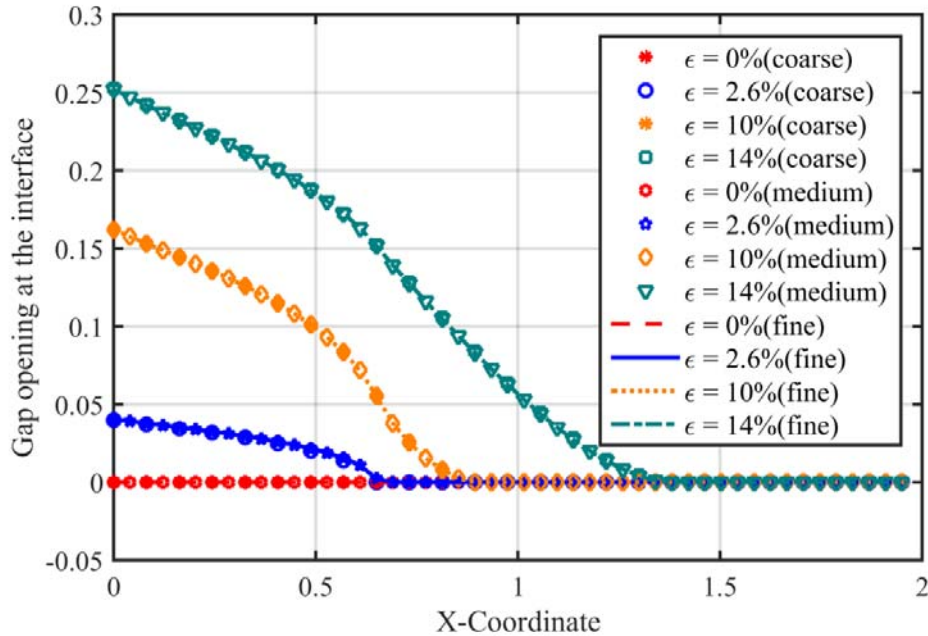(c)   (d)

Figure 14. σ_{yy} contour plots for different load steps in the tearing of bimaterial interface (Neo-Hookean material; Coarse mesh): (a) $\varepsilon = 4\%$; (b) $\varepsilon = 10\%$; (c) $\varepsilon = 14\%$; (d) $\varepsilon = 14.8\%$ (last step).

(a)

(b)

(c)

(d)

Figure 15. σ_{yy} contour plots for different load steps in the tearing of bimaterial interface (Neo-Hookean material; Medium mesh): (a) $\varepsilon = 4\%$; (b) $\varepsilon = 10\%$; (c) $\varepsilon = 14\%$; (d) $\varepsilon = 14.8\%$ (last step).

The plot of the gap/opening at the bimaterial interface for various load steps is given in Figure 16 with three different mesh refinement levels. With reference to the increasing distance of the crack

36

tip from the left end, the opening gradually increases due to the stretch applied at the bottom. The computed results from the coarse and the fine mesh match which is a numerical manifestation of the robustness of the method for relatively cruder discretizations.

Figure 16. Gap/opening evolution plots for different load steps in the tearing of bimaterial interface (Neo-Hookean material; coarse, medium and fine mesh): (a) $\varepsilon = 0\%$; (b) $\varepsilon = 2.6\%$; (c) $\varepsilon = 10\%$; (d) $\varepsilon = 14\%$;

In Figure 17, we plot the normal component of interfacial stress and the vertical gap measured at the location point of the original crack tip. The stress plot follows the traction gap relation which is shown in Figure 2.
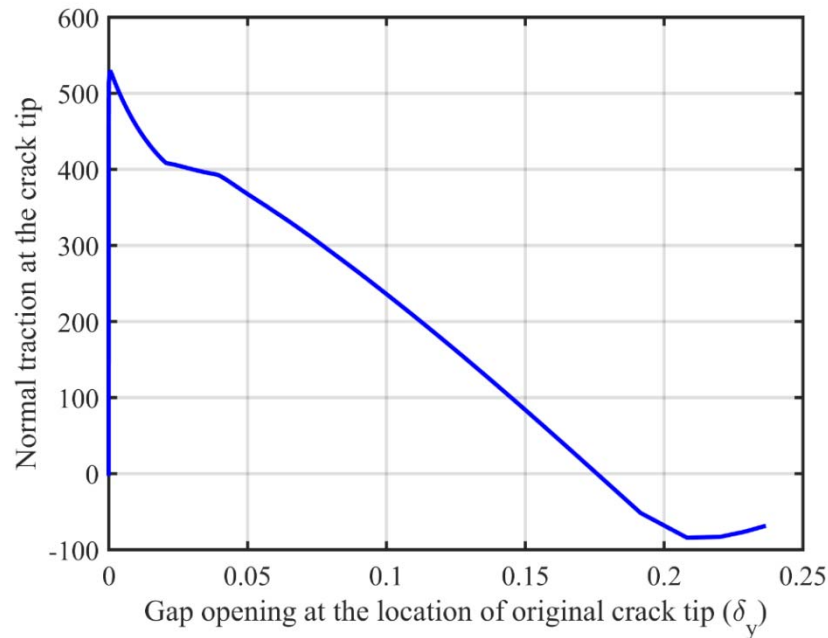
Figure 17. Normal traction at the interface vs. δ_y plot.

Figure 18 shows the spatial distribution of the fine scales along the interface during the loading process. The absolute value of the fine scales is not significant, while around the separation zone the magnitude of the fine scales is relatively high which indicates that the contribution from the fine scale model is higher in this zone. As presented in [23], these post computed fine scales also serve as a measure of local error in the solution, and the magnitude of the fine-scale error is a measure of the accuracy of the solution at the interface.
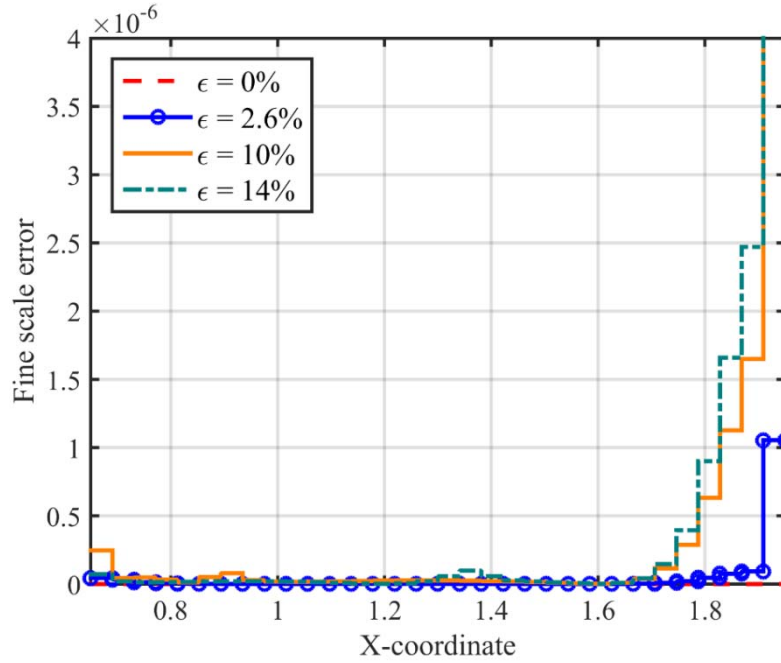
Figure 18. Fine scale error along the interface plot.

We repeat the problem where, instead of using the standard Neo-Hookean material for both stiff and soft plates, for the lower plate we use a three term Ogden-type material that matches the material response of rubber type material [24]. The strain energy function for the Ogden-type material is:

$$W\left(C\right) = \sum_{\alpha=1}^{3}\left[\frac{c_{\alpha}}{m_{\alpha}^{2}}\left(\tilde{\lambda}_{1}^{m_{\alpha}} + \tilde{\lambda}_{2}^{m_{\alpha}} + \tilde{\lambda}_{3}^{m_{\alpha}} - 3\right)\right] + \kappa U\left(J\right) \tag{87}$$

$$U\left(J\right) = \frac{1}{2}\left[\frac{1}{2}\left(J^{2}-1\right) - \ln J\right] \tag{88}$$

where $\tilde{\lambda}_{\alpha}$ is the deviatoric principal stretch. The material constants c_{α} and m_{α}, and elastic modulus and Poisson ratio which are used to compute the Bulk modulus κ are given in Table 3.

The contour plots for stress evolution and the corresponding process of tearing of bimaterial interface are shown in Figure 19 and Figure 20. It can be seen that as compared to the behavior of the standard Neo-Hookean material given in Figure 14, Ogden type material is easily stretchable that results in crack blunting and therefore prevents the crack from propagating as shown in Figure 19. Stress concentration at the crack tip and discontinuous stress field around the interface are shown in Figure 19, and these can be contrasted with the neo-Hookean material
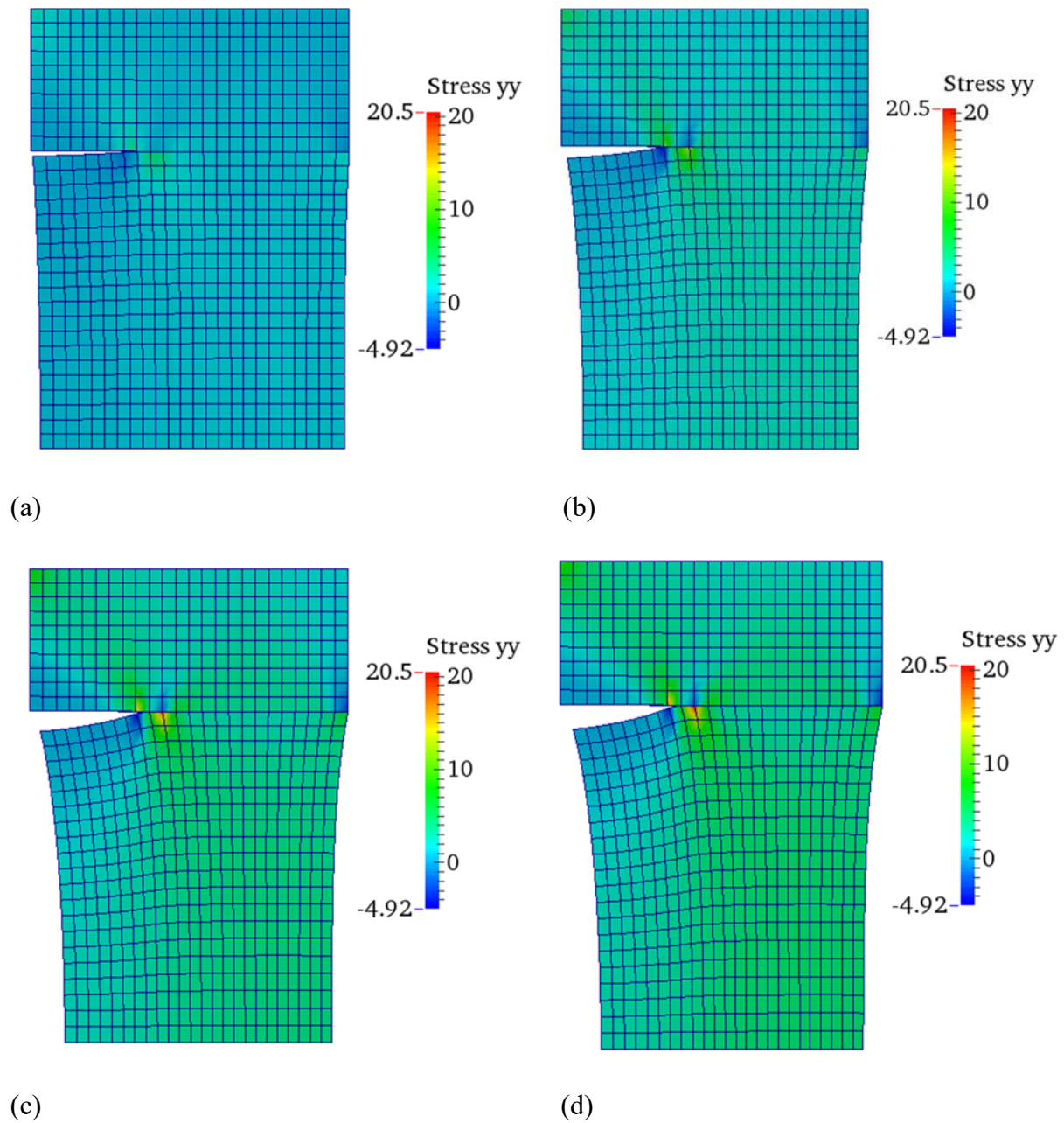
present in Figure 14.

(a)   (b)

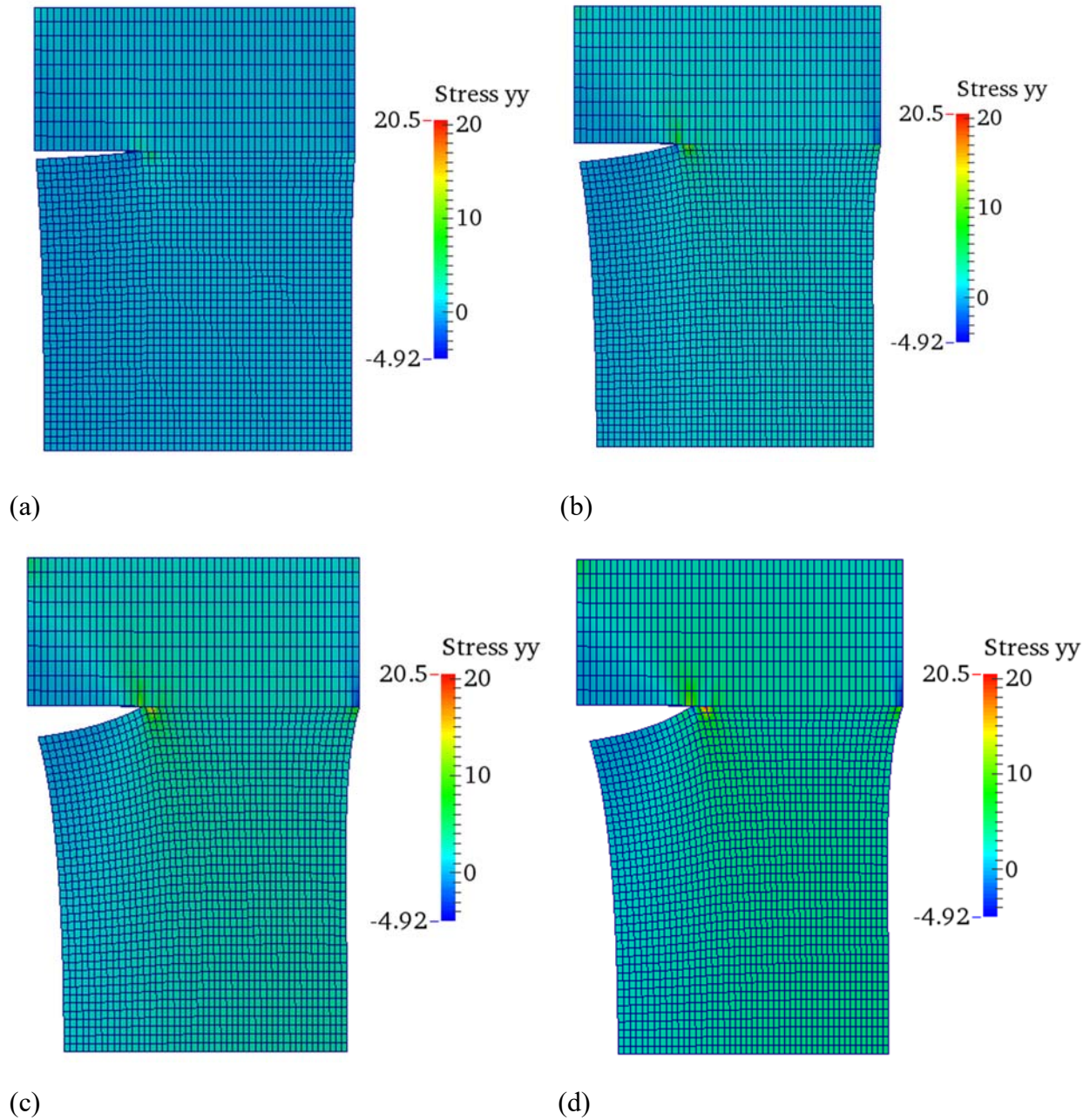(c)   (d)

Figure 19. σ_{yy} contour plots for tearing of bimaterial interface for Ogden-type material (Coarse mesh): (a) $\varepsilon = 4\%$; (b) $\varepsilon = 10\%$; (c) $\varepsilon = 16\%$; (d) $\varepsilon = 19\%$ (last step).

(a)   (b)

(c)   (d)

Figure 20. σ_{yy} contour plots for tearing of bimaterial interface for Ogden-type material (Medium mesh): (a) $\varepsilon = 4\%$; (b) $\varepsilon = 10\%$; (c) $\varepsilon = 16\%$; (d) $\varepsilon = 19\%$ (last step).

Unlike the behavior of Neo-Hookean material shown in Figure 16, Ogden type material easily undergoes large stretching. This reduces the stresses intensity at the tip of the propagating crack, and therefore triggers crack arrest. Results from the three different levels of mesh refinement are plotted, and they all converge to the response for the fine mesh, as shown in Figure 21.
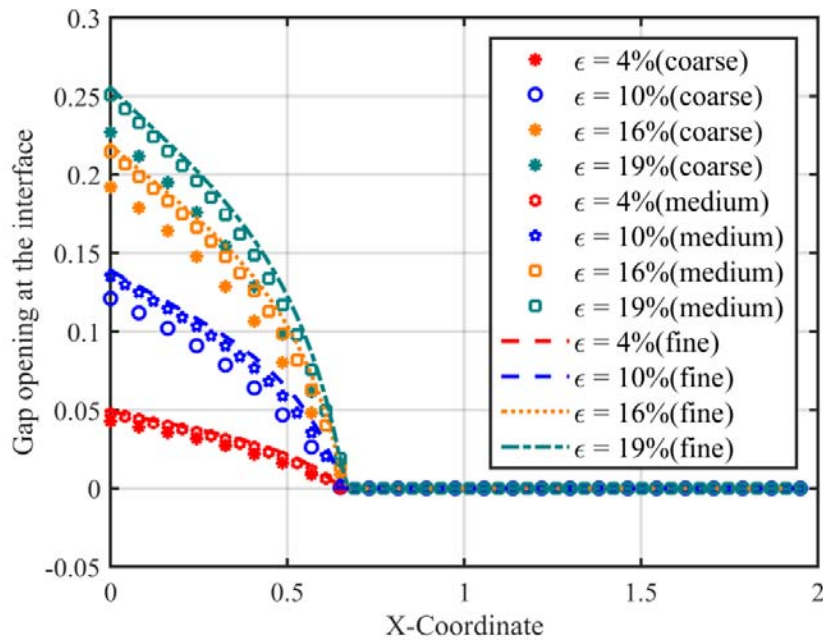
Figure 21. Gap/opening plot for tearing of bimaterial interface for Ogden-type material (Coarse, Medium and Fine mesh): (a) $\varepsilon = 4\%$; (b) $\varepsilon = 10\%$; (c) $\varepsilon = 19\%$.

Figure 22 presents the interfacial fine scales along the biomaterial interface for various applied strains, which also highlights the high accuracy of the computed solution and manifests the precise enforcement of the interfacial conditions.
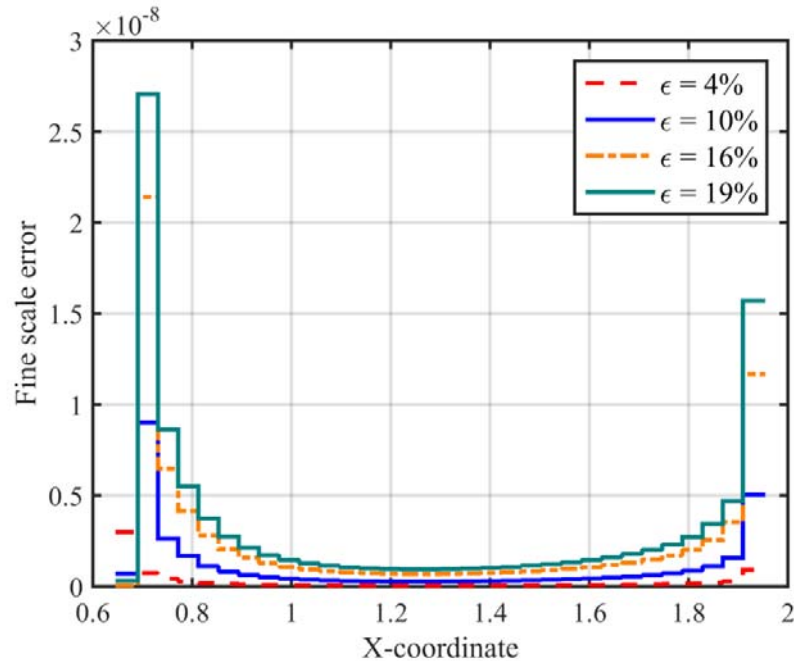
Figure 22. Fine scale error along the interface plot.

7.4.   Fiber push-out test

The last test case is a comprehensive problem that involves all three kinematic modes arising in interfacial debonding, i.e., damage in tension, damage in compression, and frictional sliding in compression. Matrix is comprised of EPON 828/DETA epoxy material and we provide a comparison of the computed solution with the numerical and experimental data presented in Bechel and Sottos [5].

Pushout tests are carried out to determine the strength of the bonded interfaces under shear stresses [5]. Consequently, this is a problem of practical interest to model fiber-matrix interface and to quantify the evolving interfacial debonding and therefore the strength and integrity of fibrous composites at microscopic level [18]. In the experimental setup, a single fiber embedded in the matrix is pressed by a punch until it is pushed out of the composite. The force-displacement history of the punch is recorded and thereafter is used to compute interface properties such as fracture toughness and the coefficient of friction [18]. A schematic cross-section of the experimental setup is shown in Figure 23. The dimensions of the specimen as shown in Figure 23 are $r_f = 0.95 \text{ mm}$, $r_m = 4.3 \text{ mm}$, $H = 5.36 \text{ mm}$, and $r_s = 1.025 \text{ mm}$.
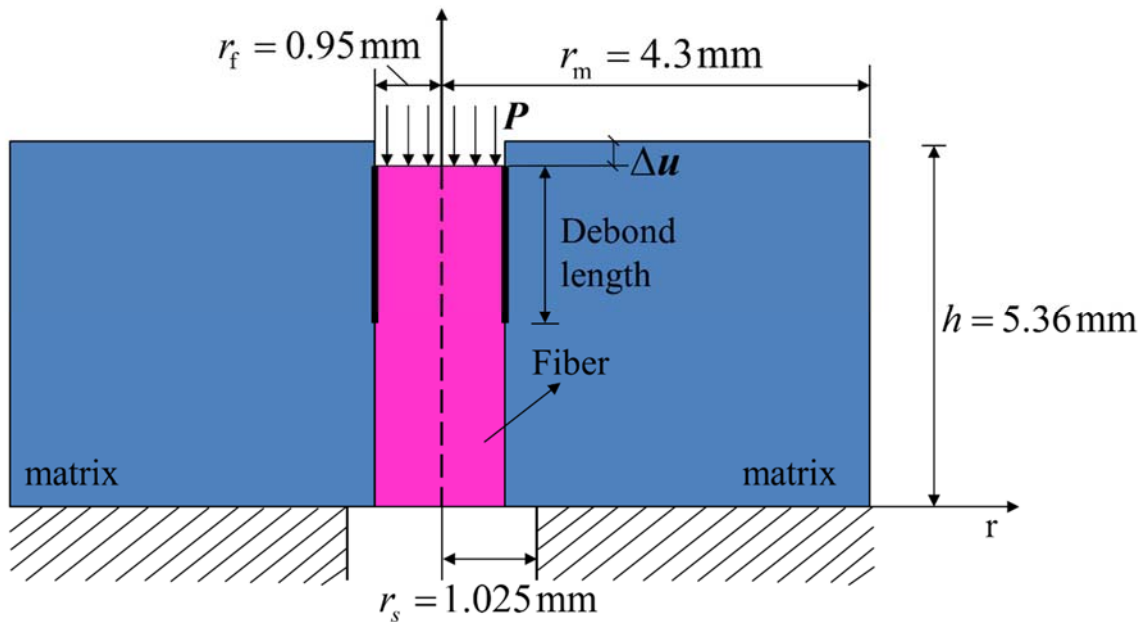
Figure 23. Pushout test problem description, cross-sectional view [5].

The three-dimensional finite element mesh is shown in Figure 24. Trilinear hexahedral elements are employed for the matrix and the fiber, and the DG method with residual gap as an internal variable is used along the composite interface. To numerically evaluate the interfacial quantities four integration points are employed in each interface "element". A quarter of the cylindrical domain is modeled with 2,125 elements in the fiber and 9,775 elements in the matrix, with 25 elements through the height of the specimen. The material properties for the fiber and matrix are listed in Table 4; critical stress and critical inelastic gap which are interface properties are taken

as $P_c = 22 \text{ N/mm}^2$ and $\delta_c = 0.011 \text{ mm}$, respectively, to match the study presented in [18,1,5].
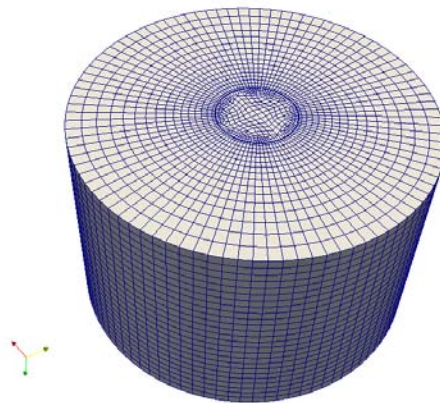

Figure 24. Mesh for the pushout test.

Table 4. Material properties of the fiber and matrix.

Material	Youngs modulus		Poisson ratio	
Matrix	$E_m \, (\text{N/mm}^2)$	4000	v_m	0.33
Fiber	$E_f \, (\text{N/mm}^2)$	2500	v_f	0.35

This simulation is performed in two steps. To model the manufacturing stage (initial stage), a constant thermal strain field equal to $\varepsilon_{th} = -0.0022$ is applied to the matrix to replicate the shrinkage effects that occur during the curing phase, and this value is an experimentally measured value reported in [5]. To model the mechanical loading stage (second stage), a prescribed displacement along the fiber axis is applied to the top surface of the fiber, representing the application of the punch load P. The maximum displacement applied is $u_y = -0.174 \, \text{mm}$. The corresponding associated force is computed by summing the reactions computed at the nodes at the top surface of the fiber.

7.4.1   Evolution of stress and interfacial damage

Contour plots of the maximum principal stress and shear stress for the two loaded configurations are presented in Figure 25 and Figure 26. The initial residual stress pattern caused by the shrinkage of the matrix is shown in Figure 25(a) and Figure 26(a). At the initial stage, due to the thermal strain ε_{th} in the matrix, the top region of the interface is under tension, which causes the debonding under tension. As can be seen in Figure 25(a) and Figure 26(a), elements at the interface near the top are undergoing relatively large positive traction that validates tangential debonding near the top of the interface. The value of the shear stress in Figure 25(b) is found to be closer to the critical stress, indicating that debonding gets triggered at the top. Also, the location of the maximum value of the shear stress tends to occur near the evolving front of the debonded interface. In Figure 25(d) and Figure 26(d) that correspond to the last step of the simulation, the computed displacement field in the fiber is shows a lack of connectivity between these two constituents. Accordingly, the force also gradually reduces and at this stage, the fiber and matrix are completely separate from each other and any remaining interfacial interaction force is due to the frictional sliding along the bimaterial interface.
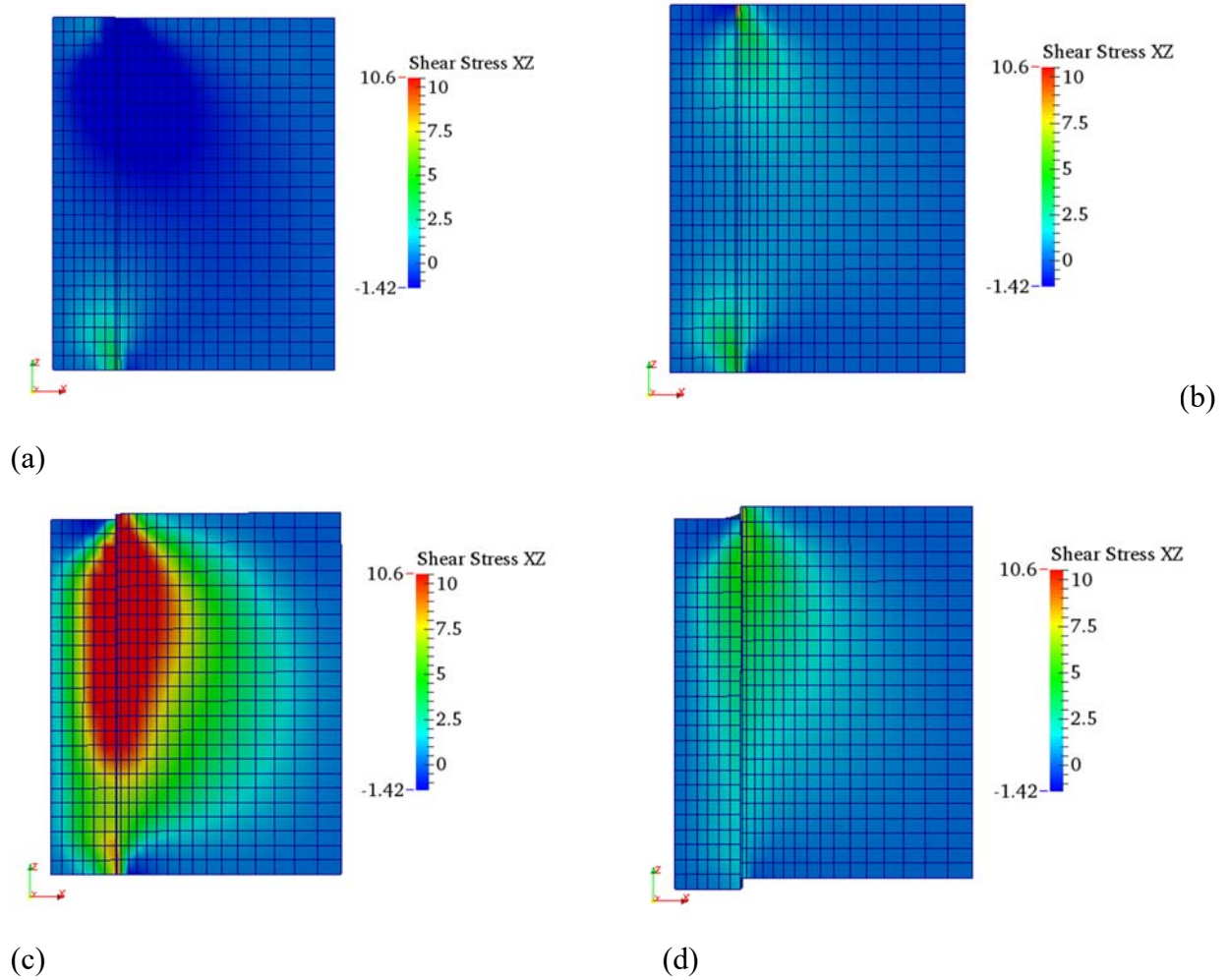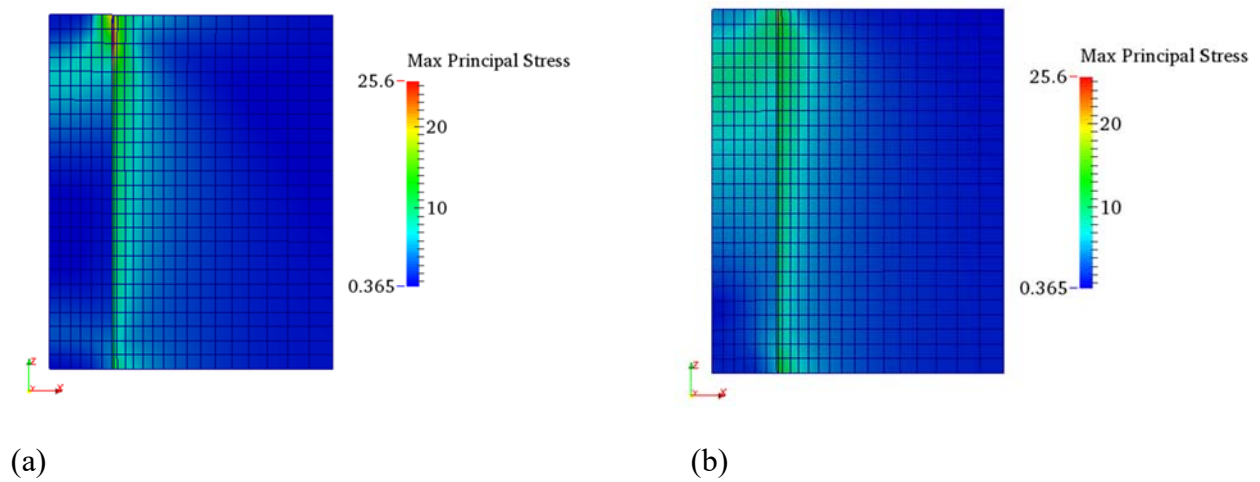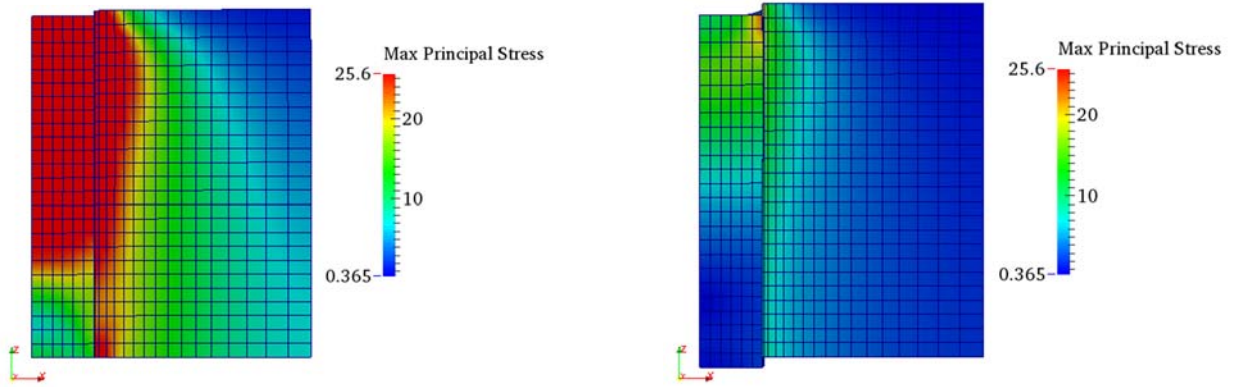
(a)

(b)

(c)

(d)

Figure 25. Shearing stress (MPa) contours at four load levels: (a) Initial step; (b) Initiation of debonding ($P = 98.62\,\mathrm{N}$); (c) Maximum sustained force ($P = 412.21\,\mathrm{N}$); (d) Final stage ($P = 105.52\,\mathrm{N}$)
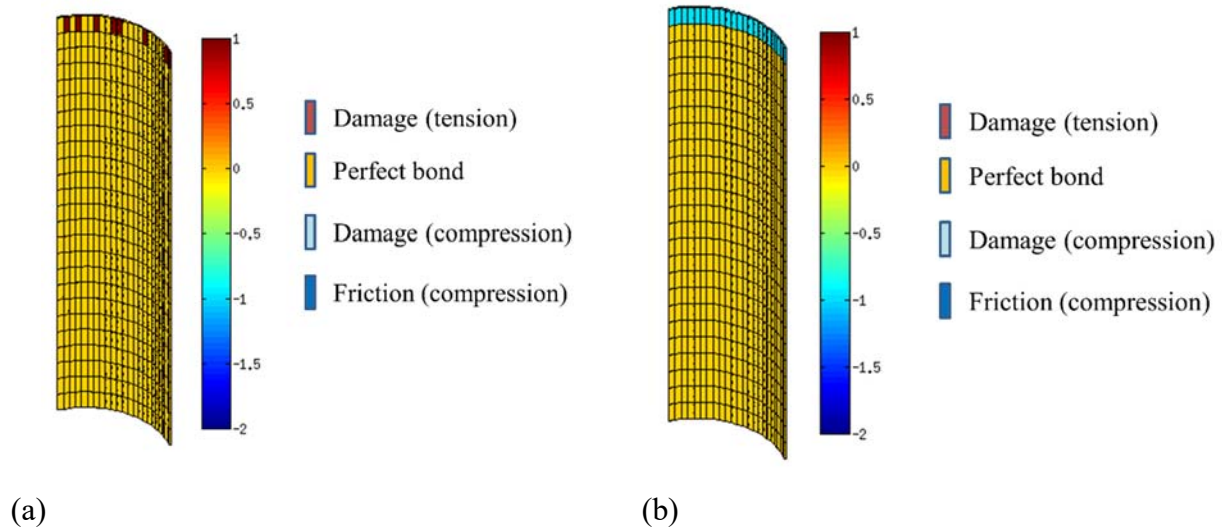

(a)

(b)

(c)   (d)

Figure 26. Maximum principal stress (MPa) distribution at four load levels: (a) Initial step; (b) Initiation of debonding ($P = 98.62\,\text{N}$); (c) Maximum sustained force ($P = 412.21\,\text{N}$); (d) Final stage ($P = 105.52\,\text{N}$)

In Figure 27, we provide this unique property of our method that can indicate the corresponding interface kinematic model that is active for any interfacial element at the different load levels. From Figure 27 (a) to Figure 27 (d), the top elements at the interface switch from damage-tension to damage-compression and finally to the frictional sliding model, which matches exactly the loading process from the initial step to the final load step.

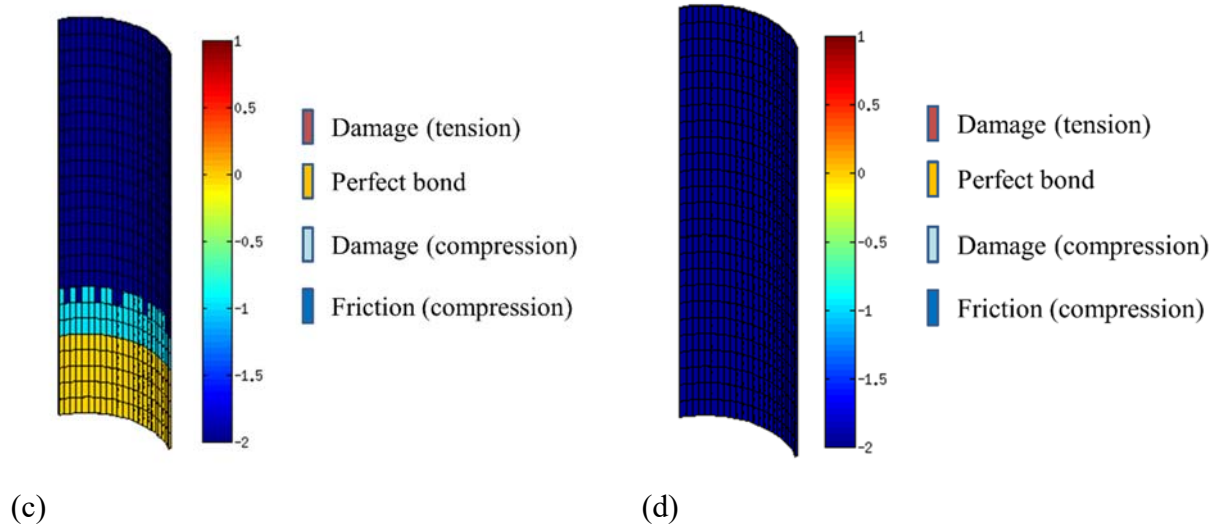(a)   (b)

(c)   (d)

Figure 27. Tracking of damage propagation at four load levels: (a) Initial step; (b) Initiation of debonding ($P = 98.62\,\text{N}$); (c) Maximum sustained force ($P = 412.21\,\text{N}$); d) Final stage ($P = 105.52\,\text{N}$)

7.4.2   Evolution of punch force and debond-length curve

The time-history of the applied punch force versus displacement at the top surface of the fiber is plotted as the red curve in Figure 28, and the results compare well with the experimental and numerical results presented in references [18,1]. The slopes of the curves in the initial loading region were computed to be approximately 8,800 N/mm. The figure shows that the proposed DG method can model debonding behavior and trace the curve successfully. As stated in Alfano [1], when the force reaches its maximum value, debond evolution becomes unstable. Thus in [1], a secant method is used to numerically model the sudden decrease in force as observed in the experiment. Unlike the method in [1], our VMDG method can model the sudden jump in the force automatically. In our method, we have the critical inelastic gap as the variable that controls the softening process in the material. Therefore, without switching to another numerical solver such as the secant method [1], a force curve with stiff slope in the softening process is obtained as shown in Figure 28, which matches well the rapid drop in force as presented in Lin [18] and Alfano [1].
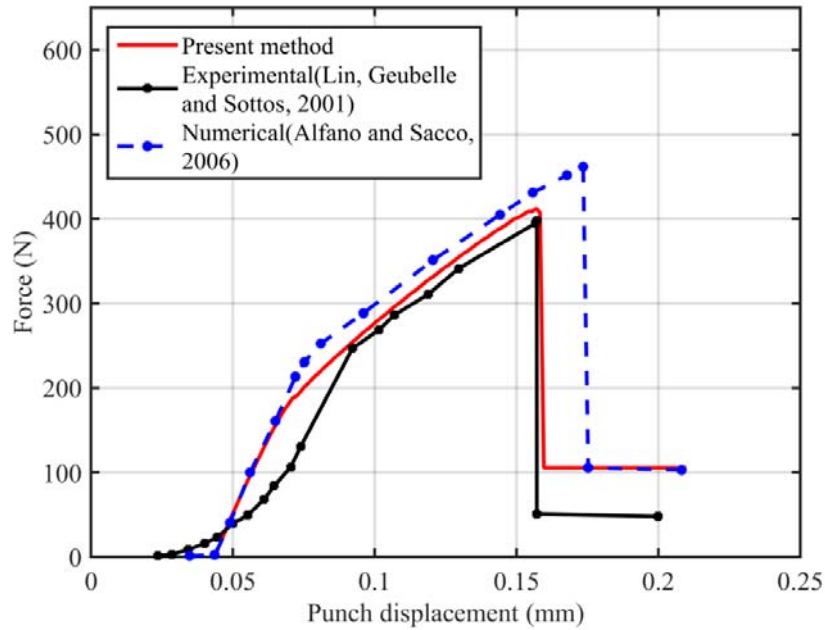
Figure 28. Force-displacement curves for mechanical stage

The relation between the debond length versus the punch displacement is shown and compared with Lin [18] and Alffano [1] in Figure 29, and a good comparison is attained.
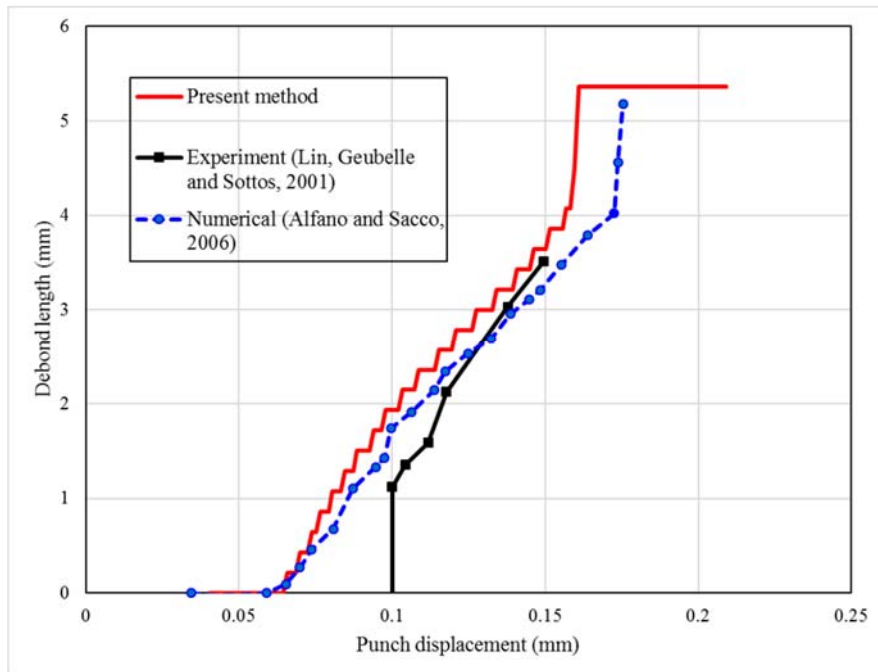

Figure 29. Debond length versus punch displacement

49

7.4.3 Parametric study

As illustrated in [18], many parameters affect the overall performance of this push-out test. For further investigation of the robustness of our method, we study the effect of different E_f / E_m ratios and friction coefficients μ_f. The force-displacement curves for different Young's modulus ratio and for different friction coefficient μ_f are given in Figure 30 and Figure 31. In Figure 30, the maximum force attained for $E_f / \mathrm{E}_m = 0.625$ and $E_f / \mathrm{E}_m = 2.5$ is in the same range while for $E_f / \mathrm{E}_m = 6$, the maximum force that the interface can sustain, drops. Likewise, the force vs. punch displacement plots for different friction coefficient are presented in Figure 31. As the friction coefficient μ_f represents the strength of the bonding at the interface between fiber and matrix, for a given punch displacement the interfacial force sustained at the interface increases as friction coefficient increases. Furthermore the punch displacement that leads to interfacial failure also increases, as shown in Figure 31.
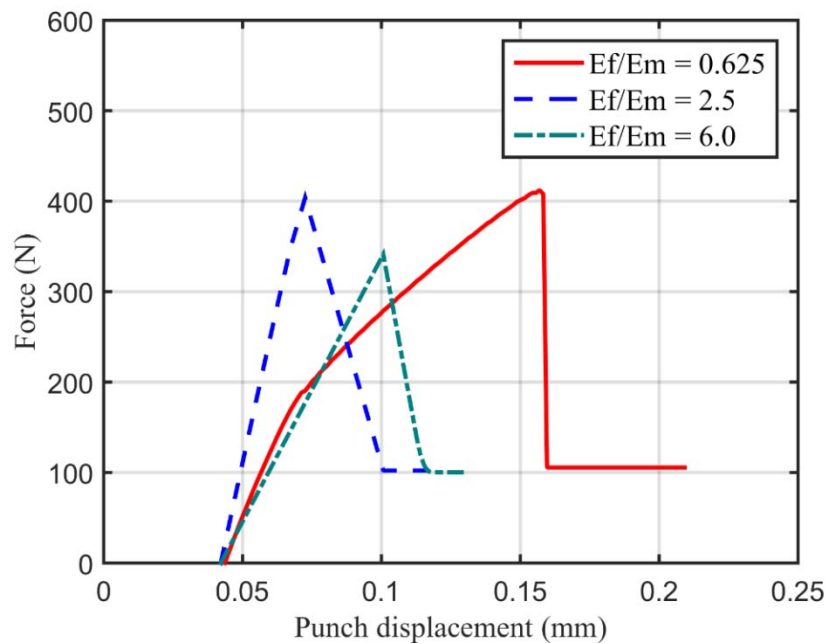

Figure 30. Force vs. punch displacement for various E_f / E_m ratio
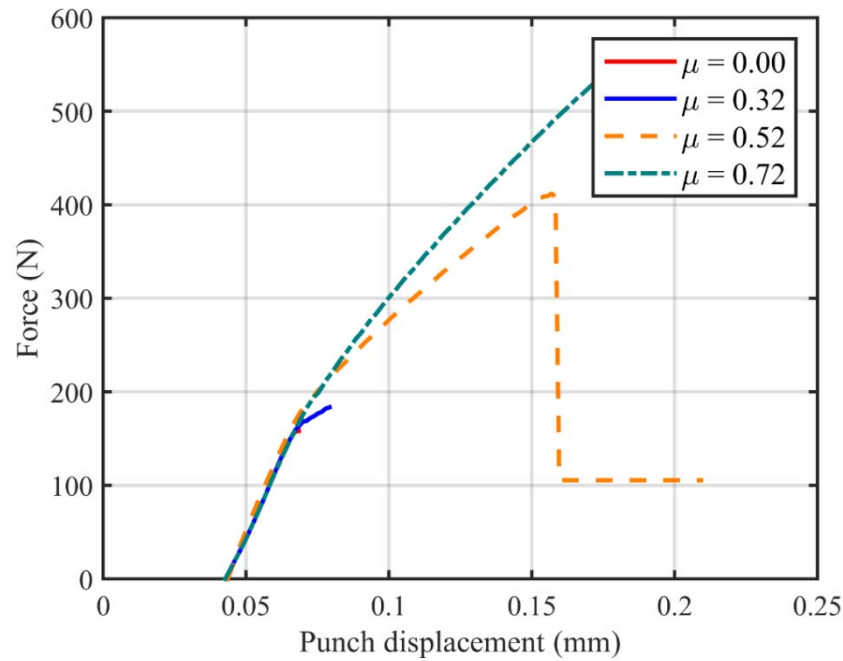
Figure 31. Force vs. punch displacement for various frictional coefficient μ_f

8. Conclusion

We have developed a Variational Multiscale DG (VMDG) formulation for strong discontinuity and interfacial debonding in multi-constituent materials at finite strains. A significant contribution of the method is a consistently derived Lagrange multiplier field as a function of interface tractions and evolving gap function. It is weighted by the evolving stability tensor which is a function of the nonlinearly evolving material and geometric parameters, thus accommodating the notions of area averaging and stress averaging. Appearance of the gap function in the expression for the Lagrange multiplier and therefore in the evolving finite-scales provides a natural mechanism to embed physics based models as well as phenomenological models for progressive failure under various loading scenarios. This is a significant contribution of the present work and sets it apart from any numerical methods that have been proposed for interfacial kinematics of finitely deforming embedded interfaces with evolving gaps and discontinuities. The proposed method allows treatment of the interface constitutive behavior through yield functions and flow rules that are inspired by the literature from plasticity. In the present method the combination of damage and friction along the debonding surfaces is easily accommodated by borrowing concepts from multi-surface plasticity. Also, rate dependency and other advanced phenomena can be easily treated in the new framework. Specially, the proposed method avoids using cohesive elements that can introduce artificial elastic interface stiffness that affects the consistency and therefore the stability of the method. With the fine-scale models

51

evolving with the material and geometric nonlinearity exhibited in the vicinity of the interface, the algorithmic interface parameters are updated continuously through the evolution of the nonlinear problem. Several interfacial kinematic modes involving tension debonding, evolution of normal gap, and compressive frictional sliding are considered and corresponding algorithmic generalizations are presented. The proposed consistent derivation that variationally embeds the interfacial kinematic models is crucial to the derivation of consistent tangent tensors that result in quadratic convergence rates when employed in the Newton Raphson method. A series of 2D and 3D benchmark problems is presented that show the numerical attributes of the method and seamlessly track the various interfacial debonding modes in the finite strain context.

Appendix A

In order to achieve quadratic convergence with the Newton-Raphson method for the nonlinear equation (85), we need consistent linearization of the term which is related to the damage part.

$$\frac{\partial}{\partial \boldsymbol{T}}\left(\Delta\gamma\boldsymbol{n}\right)=\frac{\partial\Delta\gamma}{\partial \boldsymbol{T}}\otimes\boldsymbol{n}+\gamma\frac{\partial\boldsymbol{n}}{\partial \boldsymbol{T}}=\frac{\partial\Delta\gamma}{\partial T_i}n_j+\Delta\gamma\frac{\partial n_i}{\partial T_j} \tag{89}$$

According to Section 5.1.1 and 5.2.1, the return mapping algorithms and the corresponding expression for the damage consistency parameter $\Delta\gamma$ and the unit normal $\boldsymbol{n}$ are different for different loading scenarios. Therefore, we first consider the case of damage in tension. Note that compression damage case follows a similar pattern. For the case of damage in tension, from the expressions in Box 2, the yield function f and the damage consistency parameter $\Delta\gamma$ are expressed in (67) and (68), equation (89) becomes:

$$\frac{\partial}{\partial \boldsymbol{T}}\left(\Delta\gamma\boldsymbol{n}\right)=\frac{1}{r_P-H_c}\left(\boldsymbol{I}-\frac{P_c-Q_n}{\|\boldsymbol{T}\|}\left(\boldsymbol{I}-\boldsymbol{n}\otimes\boldsymbol{n}\right)\right) \tag{90}$$

For compression friction case, the yield function and the damage consistency parameter are expressed in (77) and (79):

Thus (89) becomes:

$$\frac{\partial}{\partial \boldsymbol{T}}\left(\Delta\gamma\boldsymbol{n}\right)=\frac{1}{r_p}\left[\boldsymbol{I}+\frac{\mu_f\|T_N\|}{\|T_T\|}\left(\boldsymbol{I}-\boldsymbol{n}_T\otimes\boldsymbol{n}_T\right)\right]\left(\boldsymbol{I}-\boldsymbol{N}\otimes\boldsymbol{N}\right)+\frac{1}{r_p}\mu_f\boldsymbol{n}_T\otimes\boldsymbol{N} \tag{91}$$

References

1. G. Alfano, E. Sacco, Combining interface damage and friction in a cohesive-zone model. Int. J Numer. Methods Eng. 68 (2006) 542–582.

2. C. Annavarapu, M. Hautefeuille, J.E. Dolbow. A robust Nitsche's formulation for interface problems. Comput. Methods Appl. Mech. Eng. 225 (2012) 44-54.

3. D. N. Arnold, F. Brezzi, B. Cockburn, and L. D. Marini. Unified analysis of discontinuous Galerkin methods for elliptic problems. SIAM J. Numer. Anal. 39 (2002) 1749–1779.

4. H. J. C. Barbosa and T. J. R. Hughes. The finite element method with Lagrange multipliers on the boundary: circumventing the Babuška-Brezzi condition. Comput. Methods Appl. Mech. Eng. 85 (1991) 109–128.

5. V.T. Bechel, N.R. Sottos, A comparison of calculated and measured debond lengths from fiber push-out tests. Compos. Sci. Technol. 58 (1998) 1727–1739.

6. R. de Borst, J.J.J.C. Remmers, A. Needleman, Mesh-independent discrete numerical representaitons of cohesive-zone models. Eng. Fract. Mech. 73 (2006) 160-177.

7. G.T. Camacho, M. Ortiz. Computational modelling of impact damage in brittle materials. Int. J Solids Struct. 33 (1996) 2899-2938.

8. P. Castillo, Performance of Discontinuous Galerkin Methods for Elliptic PDEs. SIAM J Sci. Comput. 24 (2002) 524-547.

9. R. E. Ewing, J. Wang, and Y. Yang. A stabilized discontinuous finite element method for elliptic problems. Numer. Linear Algebra Appl. 10 (2003) 83–104.

10. A.T. Eyck, A. Lew, Discontinuous Galerkin methods for non-linear elasticity. Int. J Numer. Methods Eng. 67 (2006) 1204-1243.

11. A.T. Eyck, Celiker F, Lew A, Adaptive stabilization of discontinuous Galerkin methods for nonlinear elasticity: Analytical estimates. Comput. Methods Appl. Mech. Eng. 197 (2008) 2989-3000.

12. A.T. Eyck, F. Celiker, A. Lew, Adaptive stabilization of discontinuous Galerkin methods for nonlinear elasticity: Motivation, formulation, and numerical examples. Comput. Methods Appl. Mech. Eng. 197 (2008) 3605-3622.

13. P. Hansbo, M.G. Larson. Discontinuous Galerkin methods for incompressible and nearly incompressible elasticity by Nitsche's method. Comput. Methods Appl. Mech. Eng. 191 (2002) 1895-1908.

14. P. Hansbo, C. Lovadina, I. Perugia, G. Sangalli. A Lagrange multiplier method for the finite element solution of elliptic interface problems using non-matching meshes. Numer. Math. 100 (2005) 91-115.

15. P. Hansbo, K. Salomonsson. A discontinuous Galerkin method for cohesive zone modelling. Finite Elem. Anal. Des. 102-103 (2015) 1-6.

16. T.J.R. Hughes, Multiscale phenomena: Green's functions, the Dirichlet-to-Neumann formulation, subgrid scale models, bubbles and the origins of stabilized methods. Comput. Methods Appl. Mech. Eng.127 (1995) 387-401.

17. S. Li, S. Ghosh, Modeling interfacial debonding and matrix cracking in fiber reinforced composites by the extended Voronoi cell FEM. Finite Elem. Anal. Des. 43 (2007) 397-410.

18. G. Lin, P.H. Geubelle, N.R. Sottos, Simulation of fiber debonding with friction in a model composite pushout test. Int. J Solids Struct. 38 (2001) 8547-8562.

19. R. Liu, M.F. Wheeler, I. Yotov, On the spatial formulation of discontinuous Galerkin methods for finite elastoplasticity. Comput. Methods Appl. Mech. Eng. 253 (2012) 219-236.

20. E. Lorentz, A mixed interface finite element for cohesive zone models. Comput. Methods Appl. Mech. Eng. 198 (2008) 302–317.

21. A. Masud, C.L. Tham, Three-Dimensional co-rotational framework for finite deformation elasto-plastic analysis of multilayered composite shells. AIAA J. 38 (2000) 2320-2327.

22. A. Masud, T. Truster, L. Bergman, A variational multiscale a-posteriori error estimation method for mixed-form of nearly incompressible elasticity. Comput. Methods Appl. Mech. Eng. 200 (2011) 3453–3481.

23. A. Masud, T. Truster, L. Bergman, A unified formulation for interface coupling and frictional contact modeling with embedded error estimation. Int. J Numer. Methods Eng. 92 (2012) 141-177.

24. A. Masud, T. Truster, A framework for residual-based stabilization of incompressible finite elasticity: Stabilized formulations and $\bar{F}$ methods for linear triangles and tetrahedra. Comput. Methods Appl. Mech. Eng. 267 (2013) 359–399.

25. J. Mergheim, E. Kuhl, P. Steinmann, A hybrid discontinuous Galerkin/interface method for the computational modelling of failure. Comput. Methods Appl. Mech. Eng. 20 (2004) 511-519.

26. J. Mergheim, P. Steinmann, A geometrically nonlinear FE approach for the simulation of strong and weak discontinuities. Comput. Methods Appl. Mech. Eng. 195 (2006) 5037-5052.

27. L. Mu, J. Wang, Y. Wang, and X. Ye, A computational study of the weak Galerkin method for second-order elliptic equations. Numer Algor. 63 (2013) 753–777.

28. L. Mu, J. Wang, G. Wei, X. Ye, and S. Zhao, Weak Galerkin methods for second order elliptic interface problems. J. Comput. Phys. 250 (2013) 106–125.

29. L. Mu, J. Wang, and X. Ye, A weak Galerkin finite element method with polynomial reduction. J. Comput. Appl. Math. 285 (2015) 45–58.

30. V.P. Nguyen, Discontinuous Galerkin/Extrinsic cohesive zone modeling: implementation caveats and applications in computational fracture mechanics. Eng. Fract. Mech. 128 (2014) 37-68.

31. N. Nguyen-Thanh, K. Zhou, X. Zhuang, P. Areias, H. Nguyen-Xuan, Y. Bazilevs, and T. Rabczuk. Isogeometric analysis of large-deformation thin shells using RHT-splines for multiple-patch coupling. Comput. Methods Appl. Mech. Eng. 316 (2017) 1157–1178.

32. M. Prechtel, P. Ronda Leiva, R. Janisch, A. Hartmaier, G. Leugering, P. Steinmann, M. Stingl, Simulation of fracture in heterogeneous elastic materials with cohesive zone models. Int. J Fract. 168 (2011) 15-29.

33. P. Raghavan, S. Ghosh, A continuum damage mechanics model for unidirectional composites undergoing interfacial debonding. Mech. Mater. 37 (2005) 955-979.

34. J.D. Sanders, T.A. Laursen, M.A. Puso, A Nitsche embedded mesh method. Comput. Mech. 49 (2012) 243-257.

35. A. Seagraves, R. Radovitzky. Large-scale 3D modeling of projectile impact damage in brittle plates. J. Mech. Phys. Solids. 83 (2015) 48-71.

36. J. Simo, T.J.R. Hughes, Computational inelasticity 1998; Springer, New York.

37. J. Simo, T.A. Laursen, An augmented Lagrangian treatment of contact problems involving friction. Comput. Struct. 42 (1992) 97-116.

38. J. Simo, R.L. Taylor, Quasi-Incompressible finite elasticity in principal stretches. Continuum basis and numerical algorithms, Comput. Methods Appl. Mech. Eng. 85 (1991) 273-310.

39. D. Spring, O. Giraldo-Londoño, G. Paulino, A study on the thermodynamic consistency of the Park–Paulino–Roesler (PPR) cohesive fracture model, Mech. Res. Commun. Doi: 10.1016/j.mechrescom.2016.05.006.

40. C. Talon, A model of adhesion coupled to contact and friction. Eur. J Mech. A-Solids. 22 (2003) 545-565.

41. C.L. Tham, Z. Zhang and A. Masud, An elastoplastic damage model cast in a corotational kinematic framework for large deformation analysis of laminated composite shells. Comput. Methods Appl. Mech. 194 (2005) 2641-2660.

42. T. Truster, P. Chen, A. Masud, Finite strain primal interface formulation with consistently evolving stabilization. Int. J Numer. Methods Eng. 102 (2015) 278-315.

43. T. Truster, P. Chen, A. Masud, On the algorithmic and implementational aspects of a Discontinuous Galerkin method at finite strains. Comput. Math. Appl. 70 (2015) 1266-1289.

44. T. Truster, A. Masud, A Discontinuous/continuous Galerkin method for modeling of interphase damage in fibrous composite systems. Comput. Mech. 52 (2013) 499–514.

45. T. Truster, A. Masud, Primal interface formulation for coupling multiple PDEs: A consistent derivation via the Variational Multiscale method. Comput. Methods Appl. Mech. Eng. 268 (2014) 194-224.

46. T. Truster, A. Masud, Discontinuous Galerkin method for frictional interface dynamics. J. Eng. Mech. (2016) Doi: 10.1061/(ASCE)EM.1943-7889.0001142.

47. T. Truster, A stabilized, symmetric Nitsche method for spatially localized plasticity, Comput. Mech. 57 (2016) 75-103.

48. T. Truster, On interface element insertion into three-dimensional meshes, Eng. Frac. Mech. 153 (2016) 171-174.

49. Y. Wang and H. Waisman. From diffuse damage to sharp cohesive cracks: A coupled XFEM framework for failure analysis of quasi-brittle materials. Comput. Methods Appl. Mech. Eng. 299 (2016) 57–89.

50. J. Wang and X. Ye, A weak Galerkin finite element method for second-order elliptic problems. J. Comput. Appl. Math. 241 (2013) 103–115.

51. P. Wriggers, O. Scherf, Adaptive finite element techniques for frictional contact problems. Comput. Methods Appl. Mech. Eng. 151 (1998) 593–603.

52. L. Wu, D. Tjahjanto, G. Becker, A. Makradi, A. Jérusalem, L. Noels, A micro-meso-model of intra-laminar fracture in fiber-reinforced composites based on a discontinuous galerkin/cohesive zone method. Eng. Fract. Mech.. 104 (2013) 162-183.

53. Z. (Jenny) Zhang, G. H. Paulino, and W. Celes. Extrinsic cohesive modelling of dynamic fracture and microbranching instability in brittle materials. Int. J Numer. Methods Eng. 72 (2007) 893–923.

54. J. Zhao, M.A. Bessa, J. Oswald, Z.Liu, and T. Belyschko. A method for modeling the transition of weak discontinuities to strong discontinuities: from interfaces to cracks. Int. J Numer. Methods Eng. 105 (2016) 834-854.